Contents lists available at ScienceDirect

## **Composite Structures**

journal homepage: www.elsevier.com/locate/compstruct



# Revisiting multi-phase field model for FRCs using Puck theory

Pavan Kumar Asur Vijaya Kumar a<sup>1</sup>, Rafael Fleischhacker a<sup>1</sup>, Aamir Dean b,c<sup>1</sup>, Raimund Rolfes b<sup>1</sup>, Heinz E. Pettermann a<sup>1</sup>

- a Institute of Lightweight Design and Structural Biomechanics, Technische Universität Wien, Getreidemarkt 9, 1060 Vienna, Austria
- b Institute of Structural Analysis. Leibniz Universität Hannover, Appelstr. 9A, 30167 Hannover, Germany
- c School of Civil Engineering, College of Engineering, Sudan University of Science and Technology, P.O. Box 72, Khartoum, Sudan

## ARTICLE INFO

Dataset link: https://github.com/Pavan-asur/Multi-phase-field-Puck-FRC

Kevwords:

- A. Multi-phase field
- B. FRC
- C. Phase-field method
- D. ABAQUS UEL
- E. Fracture

## ABSTRACT

This article aims to revisit the multi-phase field model using the Puck failure criteria for Fiber-Reinforced Composites (FRCs). Specifically, this work proposes a robust multi-phase field formulation relying on the Puck failure criteria for triggering the fracture in fiber and the inter-fiber (matrix-dominated) separately, using two independent phase-field damage variables in a thermodynamically consistent framework. Furthermore, the formulation encompasses two distinct characteristic length scales, and a structural tensor is employed to penalize the gradient of the phase field, enhancing the accuracy of qualitative and quantitative predictions. Seven benchmark examples of unidirectional reinforced composites are utilized to demonstrate the model's predictive capabilities. The first four examples compare the proposed model with experimental results stemming from the related literature. In particular, the crack propagation with different fiber orientations, including the extreme cases involving fiber orientated parallel to the loading direction leading to debonding along the matrix and fiber interface are presented for each case. Furthermore, the last three examples serve as benchmarks to further validate the model's predictive capability. The unnotched tension specimens are examined to evaluate the effects of defects/voids on crack propagation in the FRCs in various ply orientations.

#### 1. Introduction

In recent years, there has been an unprecedented surge in the utilization of composite materials across various industries. This surge could be attributed to the unique combination of mechanical, thermal, and chemical properties. Among the composites, Fiber-Reinforced Composites (FRCs) emerged as exceptional candidates for engineering applications. The strategic alignment of the continuous fibers in various kinds of matrix material provides enhanced strength, stiffness, and damage resistance. Despite their impressive attributes, FRCs face significant challenges in predicting fracture due to their complex failure mechanisms [1].

The numerical and experimental studies of the composites are often categorized as (a) microscopic theory, (b) mesoscopic theory, and (c) macroscopic theory. Microscopic studies focus on studying composites at a scale where fiber and matrix are separated, later utilizing the results using homogenized models at larger scales. Mesoscopic models, however, consider the inter-laminar and intralaminar properties of the composites and aim to predict fracture from a single-ply point of view, consequently striking a balance between the microscopic and the larger macroscopic view. This article focuses on the mesoscopic analysis of the single plies [1].

The most common failure modes for a homogenized single-ply include inter-fiber/matrix dominated failure and fiber dominated failure. The critical energy release rate related to each failure mode is different, with magnitudes sometimes spanning across two orders. Even though inter-fiber dominated failure is the most significant failure mode, unless the loading path aligns with the fiber's direction, inter-fiber dominated failure can combine with fiber dominated failure under mixed mode loading conditions. For the sake of simplicity, inter-fiber dominated failure is refereed to as matrix failure, while the fiber dominated failure is refereed to as fiber failure herein.

The phase-field method offers an advantage in modeling composites since the gradient of the Phase-field indicates the potential crack path. Furthermore, combining the gradient with the material characterization direction can accurately account for the anisotropy. See [2–7] to name a few. The phase-field methods, in general, use Griffith's approach to fracture by smearing the crack [8–10]. Consequently, phase field methods have been able to model crack propagation, coalescence, and branching [11]. Although phase-field models are criticized for their inability to nucleate the crack without the ad hoc criteria [12,13], the phase-field model, in conjunction with other criteria, such as strength

E-mail address: pavan.kumar@tuwien.ac.at (P.K. Asur Vijaya Kumar).

Corresponding author.

criteria, emerged as an appealing computational tool for studying fracture nucleation, and propagation under various loading conditions. The phase-field methods are used to study brittle materials [14–24], dynamic fracture [15,24–28], hydrogen embrittlement [29–31], thermomechanical fracture [32–34], and composites [35–45], fatigue [46] to name a few. Several failure methods have been proposed within the context of Phase-field methods in modeling composites, such as [7,35, 40,47,48].

A recent paper by Oscar et al. [12,49] suggests that classical variational phase field models cannot predict crack nucleation. Furthermore, the study suggests that criteria for the strength (that the complete strength surface) independent of the characteristic length scale have to be included in the formulation for the phase field model to describe crack nucleation accurately. In other words, the crack nucleation has to be primarily accompanied by ad hoc criteria apart from interpolation of the characteristic length scale  $\ell$  (of phase field). Within the context of the FRCs, the phenomenological criteria such as Puck [50], Hashin [51], or physically based criteria such as [52–60] which considers the complete strength surface of the FRC has to be included in the model to account for the crack initiation and nucleation. In contrast, coalescence and crack propagation are successfully captured by the phase-field method without any ad hoc criteria.

When considering the multiple failure modes, the interaction between the failure modes, such as fiber and the inter-fiber (referred to as matrix failure which includes all the modes of Puck inter-fiber) failure, has to be considered. Consequently, the authors introduced a multi-phase field variable relying on the Puck failure criteria in [5,6]. The article uses two-phase fields to trigger failure in fiber and matrix in continuous FRCs at the ply level. The model differentiates all five modes of the Puck. Furthermore, it was demonstrated that such a model could accurately describe the failure, such as delamination migration (along with the cohesive zone model) in [6] using 44-cross ply laminates. The article in [5,6] used an invariant-based formulation without any penalty of fiber orientation direction of the phase field gradient. Furthermore, it implemented a three-layer structure utilizing UMAT and UEL of ABAOUS. Consequently, the qualitative analysis could be made more accessible, whereas the crack propagation in the angled plies was more challenging to obtain. This can be mainly attributed to the lack of directional dependent structural tensors to penalize the gradients of the phase field. Furthermore,

Another multi-phase approach in parallel was developed in [61] based on the fast Fourier transform. This method splits the energy into multiple anisotropic energies stemming from the fiber and the matrix, each represented by a separate phase field [61]. Following [5,6], Singh and Pal [42] developed a multi-phase field framework for complex fracture response. This approach has been applied to mixed mode fractures in rocks [62], elastic buckling behaviors [63], and evaluating fatigue life in composite joints [64], and explicit dynamics in FRCs [65]. The article [7] presents the most prominent failure mechanism at the material point level, and [66] combines with cohesive-like crack methods. [67] applied PF methods to three-dimensional fiber-matrix composites, [7] proposed a PF model for intralaminar and interlaminar failure in long fiber composites, [2] proposed an explicit PF model for progressive failure in FRCs. More recently, [68] presented the double-phase field model to account for multiple failure in composites. See [5.68,69] and the references thereafter for a more details.

Min et al. [70] proposed general strategies such as maximum principle stress, maximum shear stress, maximum principle strain or similar criteria to guide fracture direction in the phase-field model. But the Puck failure was not realized in the article. Furthermore, such general approach cannot be directly applied to composites due to its intrinsic material anisotropy and the distinct directional nature of the fiber and the inter-fiber failure. In this work, we address these limitations by employing orientation specific structural tensors that penalized the gradient of the phase field. This article provides a simpler mathematical model with an easy implementation in a thermodynamically consistent

framework. Consequently, the present model can now be used for both qualitative and quantitative prediction of cracks in FRCs. This article only presents the results regarding the unidirectional laminates, whereas the results regarding the isotropic and mixed laminates will be considered elsewhere. Furthermore, this article also aims to provide benchmark examples within the realm of the fracture predictions of the FRCs by combining multiple experimental results and the common numerical examples in the literature. In order to make these benchmarks more accessible, and to alleviate the reproducibility crisis, all the input files and the codes are made publicly available. As far as the authors' knowledge, no articles within the context of phase-field methods are available to successfully predict crack propagation in FRCs, which are demonstrated using all the benchmarks presented.

The article is organized as follows. Section 2 presents the modeling framework of the multi-phase field model within the context of energies. The Puck failure criteria is presented in Section 3. Furthermore, this section also provides insights into the energy considerations of the fiber and the matrix based on the Puck failure theory. Thermodynamic consistency of the formulation, along with the choice of the driving force, is presented in Section 4. It is worth noting that no tension/compression split in the formulation or the driving force is utilized in the model since the Puck failure theory can also account for compressive stress state and their subsequent failure modes. Furthermore, finite element implementation, along with the weak forms, stiffness matrix, and the residuals, are provided in Section 5. Additionally, a detailed algorithmic description of the FE implementation is also provided. Section 6 delves into numerical examples constructed using the proposed model. Moreover, this section considers seven benchmark examples, each serving a different purpose to test the ability of the proposed framework. The first part of this section focuses on comparing the proposed model with the experimental results and other numerical methods. After the scrutiny, further benchmark examples are proposed to test the model's predictive capability. Section 8 presents the conclusions of this work. Data availability provides the codes and the input files used in the article.

## 2. Variational formulation

This section introduces the variational formulation of the multiphase field model, incorporating Puck failure theory. The model uses Puck failure theory to initiate cracks, while crack propagation is governed by the phase field approach. Since the model distinguishes between fiber and inter-fiber failure, a generalized framework is initially presented. This framework is then streamlined to align with the fundamentals of the phase field method, ensuring thermodynamic consistency. Puck failure criteria is utilized using the stress state in the local ply setting, whereas the stiffness and residuals for finite element implementation are expressed in the global setting. Consequently, a unified framework addressing both global and local ply settings, including their transformations are provided. Furthermore, the details regarding the implementation are presented in Section 5.

Consider an arbitrary body in n-dimensional Euclidean space  $\mathcal B$  with its delimiting boundaries  $\partial \mathcal B$ . For every position vector  $\mathbf x \in \mathcal B$ , define a vector valued displacement field  $\mathbf u(\mathbf x,t)$  such that  $\mathbf u(\mathbf x,t): \mathcal B \times [0,t] \to \mathbb R^n$ , with  $\tau \in [0,t]$  being pseudo time. Let  $\Gamma_f$  and  $\Gamma_m$  be crack sets representing fiber failure and matrix failure, respectively, such that  $\Gamma_f, \Gamma_m \subset \mathbb R^{n-1}$ , and  $\Gamma_f \cup \Gamma_m = \Gamma$  as shown in Fig. 1.

The total energy in the system is assumed to be a consequence of the (i) applied displacement  $\bar{\mathbf{u}}$ , such that  $\mathbf{u} = \bar{\mathbf{u}}$  on  $\partial B_{\mathbf{u}}$ , (ii) traction  $\bar{\mathbf{t}} = \boldsymbol{\sigma} \cdot \mathbf{n}$  on  $\partial B_t$  with an outwards unit normal  $\mathbf{n}$ , such that  $\overline{\partial B_{\mathbf{u}} \cup \partial B_t} = \partial B$  and  $\partial B_{\mathbf{u}} \cap \partial B_t = \emptyset$ . Furthermore, (iii) body force can be applied as  $f_v : B \to \mathbb{R}^n$ . As a consequence of the applied forces on the system, the body experiences a strain field  $\varepsilon(\mathbf{x},t)$  defined as a symmetric gradient of the displacement field. i.e  $\varepsilon(\mathbf{u}) = \begin{pmatrix} \nabla \mathbf{u} + \nabla \mathbf{u}^T \\ 2 \end{pmatrix}$ . The damage in the fiber and matrix is approximated using a scalar-valued field

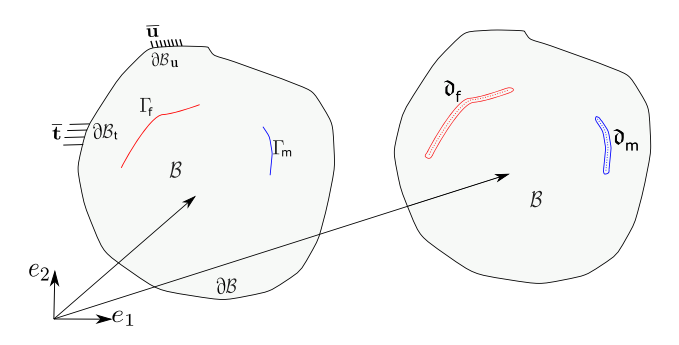


Fig. 1. Geometric description of the body under consideration: (a) sharp crack and (b) regularized crack representation.

 $\mathfrak{d}_f$ ,  $\mathfrak{d}_m$  respectively such that  $\mathfrak{d}_f(\mathbf{x},t)$ ,  $\mathfrak{d}_m(\mathbf{x},t)$ :  $B \times [0,t] \to [0,1]$ . Here,  $\mathfrak{d}=0$  refers to intact material, whereas  $\mathfrak{d}=1$  refers to as completely failed material. The variational methods to fracture for long fiber reinforced composites using the Puck failure theory can be re-iterated using additive decomposition of the total internal energy. Consequently, the total internal energy of the system can be written as a additive combination of

- 1. Strain energy  $\Psi_f$  stemming from fiber.
- 2. Strain energy  $\Psi_m$  stemming from the matrix.
- 3. Applied external energy  $\Psi_{ext}$ .
- 4. Fracture energy  $W_f$  corresponding to the fiber failure, and
- 5. Fracture energy  $W_m$  corresponding to the matrix (inter-fiber) failure.

The total internal energy density of the system using its additive constituents can be written as

$$\Psi(\mathbf{u}, \Gamma_f, \Gamma_m) = \Psi_f(\mathbf{u}) + \Psi_m(\mathbf{u}) + \mathcal{W}_f(\Gamma_f) + \mathcal{W}_m(\Gamma_m) - \Psi_{ext}(\mathbf{u}). \tag{1}$$

According to Griffith's theory, the fracture is seen as a competition between the strain energy and the energy required to create new surfaces, referred to as fracture energy. Within the context of Fiber-Reinforced Composites (FRCs) and the multi-phase field framework, the strain energy stemming from the fiber creates a new surface corresponding to fiber failure. Similarly, the strain energy stemming from the matrix creates a new surface corresponding to matrix failure. Keeping in mind Griffith's theory, the total internal energy functional can be written as

$$\Psi(\mathbf{u}, \Gamma_f, \Gamma_m) = \int_{B \setminus \Gamma_f} \Psi_f(\varepsilon) d\mathbf{x} + \int_{B \setminus \Gamma_m} \Psi_m(\varepsilon) d\mathbf{x} + G_{C,f} \mathcal{H}^{n-1}(\Gamma_f \cap \overline{B} \setminus \partial \mathcal{B}_t) + G_{C,m} \mathcal{H}^{n-1}(\Gamma_m \cap \overline{B} \setminus \partial \mathcal{B}_t) - \Psi_{ext}(\mathbf{u}).$$
(2)

Here,  $G_{C,f}$ , and  $G_{C,m}$  are the fracture energy densities corresponding to the fiber and the matrix, respectively. Whereas  $\Psi_f(\epsilon)$  and  $\Psi_m(\epsilon)$  are the undamaged strain energy densities for the fiber and matrix, respectively. The external work  $\Psi_{ext}(\mathbf{u})$  due to the applied loading can be defined as

$$\Psi_{ext}(\mathbf{u}) := \int_{\mathcal{B}} f_{v} \cdot \mathbf{u} \, d\mathbf{x} + \int_{\partial \mathcal{B}_{v}} \bar{\mathbf{t}} \cdot \mathbf{u} \, d\mathbf{S}. \tag{3}$$

The crack sets  $\Gamma_f$ , and  $\Gamma_m$  in Eq. (2) are unknown a priori. Within the context of the Phase-field models, the fracture energies for the fiber and matrix failure are approximated as

$$W_f(\Gamma_f) = \int_{\Gamma_f} G_{C,f} \, dS \approx \int_{\mathcal{B}} \frac{G_{C,f}}{4c_w} \gamma_f(\mathfrak{d}_f, \nabla \mathfrak{d}_f) d\mathbf{x}, \tag{4}$$

$$W_m(\Gamma_m) = \int_{\Gamma_m} G_{C,m} \, dS \approx \int_{\mathcal{B}} \frac{G_{C,m}}{4c_w} \gamma_m(\mathfrak{d}_m, \nabla \mathfrak{d}_m) d\mathbf{x}, \tag{5}$$

where  $\gamma_i(\mathfrak{d}_i, \nabla \mathfrak{d}_i)$  for i=(f,m) is the crack surface energy density function defined as

$$\gamma_f(\mathfrak{d}_f, \nabla \mathfrak{d}_f) = \frac{\alpha(\mathfrak{d}_f)}{\ell_f} + \ell_f \left[ \nabla \mathfrak{d}_f \cdot \mathcal{A}_f \cdot \nabla \mathfrak{d}_f \right], \tag{6}$$

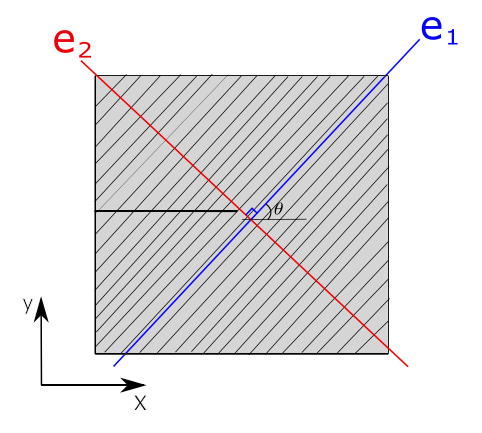


Fig. 2. Schematic diagram of the material orientations and structural tensor.

$$\gamma_{m}(\mathfrak{d}_{m}, \nabla \mathfrak{d}_{m}) = \frac{\alpha(\mathfrak{d}_{m})}{\ell_{m}} + \ell_{m} \left[ \nabla \mathfrak{d}_{m} \cdot \mathcal{A}_{m} \cdot \nabla \mathfrak{d}_{m} \right]. \tag{7}$$

Here,  $c_w := \int_0^s \sqrt{\alpha(s)} ds$  is the normalization parameter. In line with the AT2 model, the distribution of each phase-field variable is achieved by choosing the geometric crack function as  $\alpha(\mathfrak{d}_i) = \mathfrak{d}_i^2$  (i = f, m). Notice that  $\alpha : [0,1] \to [0,1]$ . Furthermore,  $\mathcal{A}_f$ , and  $\mathcal{A}_m$  is a second order structural tensor defined as

$$A_f = e_2 \otimes e_2, \qquad A_m = e_1 \otimes e_1, \tag{8}$$

where  $e_1$  is the principle material direction 1 aligned with the fiber orientation. Whereas  $e_2$  is the transverse in-plane orientation with respect to the fiber, perpendicular to  $e_1$ . For the fiber orientation of  $\theta$  from the global X- co-ordinate, the material basis functions  $e_1$ , and  $e_2$  are given by

$$e_1 = \begin{bmatrix} \cos \theta \\ \sin \theta \end{bmatrix}$$
, and  $e_2 = \begin{bmatrix} -\sin \theta \\ \cos \theta \end{bmatrix}$ . (9)

Consequently, the structural tensors  $\mathcal{A}_f$ , and  $\mathcal{A}_m$  adjust the non-local part of the fracture energy to penalize the material orientations in the fiber and the matrix respectively.

The structural tensor was first introduced in [7]. The structural tensor for the matrix was modified to include the material orientation to penalize the inter-fiber-dominated cracks introduced in [2]. On the contrary, this article uses two different structural tensors corresponding to the fiber and the inter-fiber/matrix. While using a structural tensor for the matrix is justified in [2], Appendix A provides further evidence by comparing the effects of the structural tensor. Furthermore, Fig. 2 presents the schematic diagram of the material direction  $e_1$ ,  $e_2$ . The material directions can also be seen as the projection of the fiber orientation onto the global coordinates.

According to Puck's failure criteria, in most cases, the fracture plane in the fiber is approximately perpendicular to the fiber direction. Consequently, the fiber failure is restricted to the direction perpendicular to the fiber [50]. Most of the failures are inter-fiber-dominated, especially in the unidirectional plies, unless the load application aligns with the fiber orientation. When the fiber failure is dominant, the structural tensor corresponding to the fiber becomes helpful in obtaining the crack propagation. Appendix B compares the two models with and without the fiber structural tensor. Specifically, the fiber-dominated cracks tend to smear more in the absence of the fiber structural tensor. These effects become prominent in the presence of multiple modes of failure. The analysis of the laminates suggests that using a structural tensor for fiber-dominated failure better captures the interaction between fiber and inter/fiber damage. The laminate results are omitted here and will be presented in another article.

Notice that due to the addition of the structural tensor in Eqs. (6) and (7), the gradients are penalized. In a two-dimensional setting, the

phase field gradient is represented by  $\nabla \mathfrak{d} = [\nabla_x \mathfrak{d}, \nabla_u \mathfrak{d}]$ . Consequently, due to the structural tensor, the non-local part of the surface energy can be written as  $G_c \ell_c [\nabla_x \mathfrak{d} \cdot \cos^2(\theta) + \nabla_y \mathfrak{d} \cdot \sin^2(\theta) \pm 2\cos(\theta)\sin(\theta) \cdot \nabla_x \mathfrak{d} \nabla_y \mathfrak{d}]$ . This introduces an extra term  $2G_c\ell_c\cos(\theta)\sin(\theta)\cdot\nabla_x\delta\nabla_y\delta$ . Recalling that  $\theta$  is the fiber orientation, this term is maximum when the  $\theta = 45^{\circ}$ , and reduces as the  $\theta \to 0^{\circ}, 90^{\circ}$ . Consequently, it introduces a thick bank of cracks when the  $\theta = 45^{\circ}$  can be observed in all the numerical examples throughout this article. In order to avoid spurious crack widths, one can consider the length scale dependent on the fiber orientation. In order to have a fair comparison of the results, the length scale is considered constant in this article, independent of the fiber orientation. However,

 $\bar{\ell} = \frac{\ell}{2\cos\theta\sin\theta} \text{ can also be considered.}$  Note that Puck failure theory is mainly based on the stress-field  $\sigma$  in principle material orientation (fiber orientation). In contrast, the solution to the weak forms, including elemental stiffness, residual vectors are computed globally. Consequently, a global and local coordinate system is introduced in the sequel. The quantities in the (local) principle material orientation are referred to as  $(\cdot)^{\mathcal{L}}$ , whereas the global orientation is represented as  $(\cdot)^{\mathcal{G}}$ . Within this context, the transformation from local to global coordinates and vice versa is obtained using the following transformation matrix R according to [71–74] given as

$$\mathcal{R} = \begin{bmatrix} \cos^2 \theta & \sin^2 \theta & 2\cos \theta \sin \theta \\ \sin^2 \theta & \cos^2 \theta & -2\cos \theta \sin \theta \\ -\cos \theta \sin \theta & \cos \theta \sin \theta & \cos^2 \theta - \sin^2 \theta \end{bmatrix}. \tag{10}$$

$$\boldsymbol{\varepsilon}^{\mathcal{L}} = \left(\mathcal{R}^{-1}\right)^{T} \cdot \boldsymbol{\varepsilon}^{\mathcal{G}}.\tag{11}$$

The constitutive stiffness matrix  $\mathbb{C}^{\mathcal{L}}$  can be written in the global setting

$$\mathbb{C}^{\mathcal{G}} = \mathcal{R}^{-1} \cdot \mathbb{C}^{\mathcal{L}} \cdot \left(\mathcal{R}^{-1}\right)^{T}. \tag{12}$$

As a consequence, the stress in the global coordinates can be computed

$$\sigma^{\mathcal{G}} = \mathbb{C}^{\mathcal{G}} \cdot \epsilon^{\mathcal{G}},\tag{13}$$

and in the local form as

$$\sigma^{\mathcal{L}} = \mathcal{R} \cdot \sigma^{\mathcal{G}}.\tag{14}$$

Furthermore, strain energy density contribution associated with the fiber can be written as

$$\Psi_f(\mathbf{u}, \mathfrak{d}) = g(\mathfrak{d}) \frac{1}{2} \epsilon^{\mathcal{L}} : \mathbb{C}_f^{\mathcal{L}} : \epsilon^{\mathcal{L}}, \tag{15}$$

$$\mathbb{C}_f^{\mathcal{L}} = \begin{bmatrix} C_{11} & 0 & 0 \\ 0 & 0 & 0 \\ 0 & 0 & 0 \end{bmatrix},$$
(16)

with  $C_{11}=\frac{E_{11}}{1-\nu_{12}\nu_{21}}$ . Similarly, the strain energy density contribution associated with the matrix takes the form

$$\Psi_{m}(\mathbf{u},\mathfrak{d}) = g(\mathfrak{d})\frac{1}{2}\boldsymbol{\varepsilon}^{\mathcal{L}} : \mathbb{C}_{m}^{\mathcal{L}} : \boldsymbol{\varepsilon}^{\mathcal{L}}, \tag{17}$$

$$\mathbb{C}_{m}^{\mathcal{L}} = \begin{bmatrix} 0 & C_{12} & 0 \\ C_{12} & C_{22} & 0 \\ 0 & 0 & C_{33} \end{bmatrix},$$
(18)

with  $C_{12}=\frac{v_{12}E_{11}}{1-v_{12}v_{21}}$ ,  $C_{22}=\frac{E_{22}}{1-v_{12}v_{21}}$ , and  $C_{33}=g_{12}$ . Here  $E_{11}$ ,  $E_{22}$ , and  $g_{12}$  are the longitudinal, transverse and shear modulus respectively, whereas  $v_{12}$ , and  $v_{21}=v_{12}\frac{E_{11}}{E_{22}}$  are the Poisons's ratio. Furthermore,  $g(\mathfrak{d})$  is the degradation function, whose specific details are presented in the sequel.

The total energy of the systems in Eq. (2) can be written as

$$\Psi(\mathbf{u}, \mathfrak{d}_{f}, \mathfrak{d}_{m}) = \int_{\mathcal{B}} g(\mathfrak{d}) \frac{1}{2} \boldsymbol{\varepsilon}^{\mathcal{L}} : \mathbb{C}_{f}^{\mathcal{L}} : \boldsymbol{\varepsilon}^{\mathcal{L}} d\mathbf{x} 
+ \int_{\mathcal{B}} g(\mathfrak{d}) \frac{1}{2} \boldsymbol{\varepsilon}^{\mathcal{L}} : \mathbb{C}_{m}^{\mathcal{L}} : \boldsymbol{\varepsilon}^{\mathcal{L}} d\mathbf{x} - \Psi_{ext}(\mathbf{u}) 
+ \int_{\mathcal{B}} \left[ G_{C,f} \frac{\alpha(\mathfrak{d}_{f})}{\ell_{f}} + \ell_{f} \left[ \nabla \mathfrak{d}_{f} \cdot \mathcal{A}_{f} \cdot \nabla \mathfrak{d}_{f} \right] \right] d\mathbf{x} 
+ \int_{\mathcal{B}} \left[ G_{C,m} \frac{\alpha(\mathfrak{d}_{m})}{\ell_{m}} + \ell_{m} \left[ \nabla \mathfrak{d}_{m} \cdot \mathcal{A}_{m} \cdot \nabla \mathfrak{d}_{m} \right] \right] d\mathbf{x}.$$
(20)

Note that, due to the additive decomposition of the strain energies and the fact that all the strain energies are in local-material orientation, the total internal energy in the compact notation takes the form

$$\Psi(\mathbf{u}, \mathfrak{d}_{f}, \mathfrak{d}_{m}) = \int_{\mathcal{B}} g(\mathfrak{d}) \frac{1}{2} \boldsymbol{\epsilon}^{\mathcal{L}} : \mathbb{C}^{\mathcal{L}} : \boldsymbol{\epsilon}^{\mathcal{L}} d\mathbf{x} - \Psi_{ext}(\mathbf{u}) 
+ \int_{\mathcal{B}} \left[ G_{C,f} \frac{\alpha(\mathfrak{d}_{f})}{\ell_{f}} + \ell_{f} \left[ \nabla \mathfrak{d}_{f} \cdot \mathcal{A}_{f} \cdot \nabla \mathfrak{d}_{f} \right] \right] d\mathbf{x} 
+ \int_{\mathcal{B}} \left[ G_{C,m} \frac{\alpha(\mathfrak{d}_{m})}{\ell_{f}} + \ell_{m} \left[ \nabla \mathfrak{d}_{m} \cdot \mathcal{A}_{m} \cdot \nabla \mathfrak{d}_{m} \right] \right] d\mathbf{x}.$$
(21)

Here,  $\mathbb{C}^{\mathcal{L}}$  is the total constitutive stiffness of the FRC that reads

$$\mathbb{C}^{\mathcal{L}} = \mathbb{C}_f^{\mathcal{L}} + \mathbb{C}_m^{\mathcal{L}},\tag{23}$$

leading to

$$\mathbb{C}^{\mathcal{L}} = \begin{bmatrix}
C_{11}^{\mathcal{L}} & C_{12}^{\mathcal{L}} & 0 \\
C_{12}^{\mathcal{L}} & C_{22}^{\mathcal{L}} & 0 \\
0 & 0 & C_{33}^{\mathcal{L}}
\end{bmatrix}.$$
(24)

Furthermore, due to the multiple phase fields, the total constitutive stiffness of the damaged material  $\tilde{\mathbb{C}}^{\mathcal{L}}$  takes the form

$$\tilde{\mathbb{C}}^{\mathcal{L}} = g(\mathfrak{d})\mathbb{C}_f^{\mathcal{L}} + g(\mathfrak{d})\mathbb{C}_m^{\mathcal{L}},\tag{25}$$

$$\tilde{\mathbb{C}}^{\mathcal{L}} = \begin{bmatrix} g_f \\ g_m \\ \min\{g_f, g_m\} \end{bmatrix}^T \cdot \begin{bmatrix} C_{11}^{\mathcal{L}} & C_{12}^{\mathcal{L}} & 0 \\ C_{12}^{\mathcal{L}} & C_{22}^{\mathcal{L}} & 0 \\ 0 & 0 & C_{33}^{\mathcal{L}} \end{bmatrix} \\
= \begin{bmatrix} g_f C_{11}^{\mathcal{L}} & g_m C_{12}^{\mathcal{L}} & 0 \\ g_m C_{12}^{\mathcal{L}} & g_m C_{22}^{\mathcal{L}} & 0 \\ 0 & 0 & \min\{g_f, g_m\} C_{33}^{\mathcal{L}} \end{bmatrix}.$$
(26)

Here,  $g_f = (1 - \mathfrak{d}_f)^2$ , and  $g_m = (1 - \mathfrak{d}_m)^2$  in line with standard AT2 formulation [25], such that  $g_i(0) = 1$ ,  $g_i(1) = 0$ , and  $\frac{dg_i}{d\theta_i} \ge 0$  for i = f, m. Consequently, the degraded stresses due to the damage in the local and the global reference system take the form

$$\tilde{\boldsymbol{\sigma}}^{\mathcal{L}} = g(\mathfrak{d})^T \cdot \boldsymbol{\sigma}^{\mathcal{L}}; \qquad \tilde{\boldsymbol{\sigma}}^{\mathcal{G}} = \mathcal{R}^{-1} \cdot \tilde{\boldsymbol{\sigma}}^{\mathcal{L}}. \tag{27}$$

## 3. Puck failure criteria

The initiation of the damage relies on the Puck failure theory [50]. Puck failure criteria distinguish the fiber dominated and (matrix) interfiber dominated failure independent of each other. Consequently, the damage can be initiated using the Puck failure criteria, and the evolution of the damage can be performed using the phase-field approach. In a two-dimensional setting, || (subscript 1) is used to represent the fiber direction, whereas ⊥ (subscript 2 and subscript 3) represents the direction normal to fiber direction in plane and out of plane respectively, for the ply-coordinates in a local setting  $0 - \mathbf{e}_1 - \mathbf{e}_2 - \mathbf{e}_3$ .

Puck failure theory distinguishes five modes of failure. They are (i) fiber failure in tension, (ii) fiber failure in compression, (iii) Mode-A (transverse tension) in the matrix, (iv) Mode-B (transverse compression) in the matrix, and (v) Mode-C (out of plane transverse compression) in the matrix. Furthermore, each failure mode is triggered based on an energetic consideration that the exposure factor reaches 1. Consequently, due to the multi-phase field framework, exposure factors stemming from each mode are named separately to distinguish the failure mode in the presented model.

The modulus  $E_{11}$ ,  $E_{22}$ , and  $E_{12}$  are the longitudinal and shear modulus, respectively, in the local ply orientation. Furthermore,  $R_{11}^T$ ,  $R_{22}^T$ , and  $R_{12}$  stands for the tensile longitudinal strength in fiber direction and transverse tensile strengths, respectively. Whereas  $R_{11}^C$  and  $R_{22}^C$  represent the compressive strength in the fiber direction and the direction transverse to the fiber. The major Poisson's ratios are written as  $v_{12}$ , and  $v_{23}$ . Additionally  $P_{21}^+$ ,  $P_{21}^-$ ,  $P_{22}^+$ ,  $P_{22}^-$  are the matrix inclination parameters. As a consequence of the strength considerations in all modes, Puck failure theory considers the entire strength surface, see [5,50] for more details.

## 3.1. Fiber failure

Within the context of fiber dominated failure, fracture is triggered by evaluating the so-called failure exposure factor (material efforts) in each of the identified failure mechanisms. The exposure factor relates the length of pseudo  $\varpi$ , and the corresponding material fracture vector  $\varpi_{fr}$ , i.e.  $F_i = |\varpi|/|\varpi_{fr}|$ , see [75]. The failure is initiated when the  $F_i$  reaches the value 1.

With the stress in the local coordinates, the fiber failure exposure factor  $F_f^T$  in tension can be defined as the ratio of the stress in the fiber to the strength of the fibers, written as

$$F_f^T = \frac{\sigma_{11}^{\mathcal{L}}}{R_{11}^T}, \quad \text{if} \quad \sigma_{11}^{\mathcal{L}} > 0.$$
 (28)

Similarly, the fiber failure expose factor in compression takes the form

$$F_f^C = \sqrt{\left(\frac{\sigma_{11}^L}{R_{11}^C}\right)^2 + \alpha \left(\frac{\sigma_{12}^L}{R_{12}}\right)^2} \quad \text{if} \quad \sigma_{11}^L < 0.$$
 (29)

where  $\alpha \in [0, 1]$  is the shear influence parameter for the compressive fiber failure.

#### 3.2. Matrix failure

The exposure factor corresponding to matrix dominated failure can be distinguished based on the Mode of fracture. If  $\sigma_{22}^{\mathcal{L}} > 0$ , the exposure factor in Mode-A in tension for the matrix takes the form

$$F_m^T = \sqrt{\left(\frac{\sigma_{12}^{\mathcal{L}}}{R_{12}}\right)^2 + \left(1 - P_{21}^+ \cdot \frac{R_{22}^T}{R_{12}}\right)^2 + \left(\frac{\sigma_{22}^{\mathcal{L}}}{R_{22}^T}\right)^2 + \frac{P_{21}^+ \sigma_{22}^{\mathcal{L}}}{R_{12}}}.$$
 (30)

Mode B corresponds to the transverse compressive stress with a longitudinal shear stress below a fracture resistance. The exposure factor for the Mode-B matrix fracture is triggered, if the stress state fulfills  $\sigma_{22}^{\mathcal{L}} < 0$  as well as

$$\left[ \left| \frac{\sigma_{22}^{\mathcal{L}}}{\sigma_{12}^{\mathcal{L}}} \right| > 0 \right] \&\& \left[ \left| \frac{\sigma_{22}^{\mathcal{L}}}{\sigma_{12}^{\mathcal{L}}} \right| < \left| \frac{R_{22}^a}{R_{12}^c} \right| \right], \tag{31}$$

where 
$$R_{22}^a = \frac{R_{12}}{2P_{21}^-} \left\{ \sqrt{1 + 2P_{21}^- \frac{R_{22}^C}{R_{12}}} - 1 \right\}$$
, and  $R_{12}^c = R_{12} \sqrt{1 + 2P_{22}^-}$ . The

exposure factor for the compression in Puck Mode-B takes the form

$$F_m^C = \sqrt{\left(\frac{\sigma_{12}^L}{R_{12}}\right)^2 + \left(P_{21}^- \cdot \frac{\sigma_{22}^L}{R_{12}}\right)^2 + \frac{P_{21}^- \sigma_{22}^L}{R_{12}}}.$$
 (32)

Similarly, if the stress

$$\left[ \left| \frac{\sigma_{12}^{\mathcal{L}}}{\sigma_{22}^{\mathcal{L}}} \right| > 0 \right] \&\& \left[ \left| \frac{\sigma_{12}^{\mathcal{L}}}{\sigma_{22}^{\mathcal{L}}} \right| < \left| \frac{R_{12}^{e}}{R_{22}^{e}} \right| \right], \tag{33}$$

is satisfied. A transverse compressive stress state with a longitudinal shear stress that is sufficiently high to induce fracture on an inclined plane to the fiber axis is associated with mode-C matrix failure. The compression exposure factor corresponding to the Puck Mode-C matrix failure can be written as

$$F_m^C = \left(\frac{\sigma_{12}^L}{2(1 + P_{22}^-)R_{12}}\right)^2 - \left(\frac{\sigma_{22}^L}{R_{22}^C}\right)^2 \frac{R_{22}^C}{\sigma_{22}^L}.$$
 (34)

Assuming that the Puck failure criteria is met for the stress state of  $\sigma_{+}^{\mathcal{L}}$ , the energy associated with fiber and the matrix during the Puck failure initiation (with one or multiple modes) can be computed as

$$\Psi_{f,0} = \begin{cases} \frac{1}{2} \sigma_{11}^{\mathcal{L}} \epsilon_{11}^{\mathcal{L}} & \text{if } F_f^T, F_f^C = 1\\ 0 & \text{if } F_f^T, F_f^C < 1, \end{cases}$$
 (35)

$$\Psi_{m,0} = \begin{cases} \frac{1}{2} \left( \sigma_{22}^{\mathcal{L}} \epsilon_{22}^{\mathcal{L}} + \sigma_{12}^{\mathcal{L}} \epsilon_{12}^{\mathcal{L}} \right) & \text{if } F_m^T, F_m^C = 1\\ 0 & \text{if } F_m^T, F_m^C < 1. \end{cases}$$
(36)

## 4. Thermodynamic consistency and driving force

Assuming the isothermal conditions, the second law of thermodynamics, which ensures the consistency of the formulation takes the form

$$\mathcal{D} = [\boldsymbol{\sigma} : \dot{\boldsymbol{\varepsilon}}] - \partial_{\mathcal{I}} \boldsymbol{\Psi} : \mathcal{I} \ge 0, \tag{37}$$

where  $\mathcal{I}$  is the set of internal variables, and  $(\dot{x}) = \frac{d(x)}{dt}$  is the time derivative. Setting the internal variables  $\mathcal{I}$  as a triplet  $(\mathbf{u}, \mathfrak{d}_f, \mathfrak{d}_m)$ , and their respective gradients, the Clausius–Duhem Inequality in Eq. (37) can be written as

$$\mathcal{D} = \left(\sigma - \frac{\partial \Psi}{\partial \varepsilon}\right)\dot{\varepsilon} - \left(\frac{\partial \Psi}{\partial \mathfrak{d}_f}\dot{\mathfrak{d}}_f + \frac{\partial \Psi}{\partial \nabla \mathfrak{d}_f}\nabla\dot{\mathfrak{d}}_f\right) - \left(\frac{\partial \Psi}{\partial \mathfrak{d}_m}\dot{\mathfrak{d}}_m + \frac{\partial \Psi}{\partial \nabla \mathfrak{d}_m}\nabla\dot{\mathfrak{d}}_m\right) \geq 0. \tag{38}$$

Since  $\sigma = \frac{\partial \Psi}{\partial \varepsilon} = \tilde{\mathbb{C}}^{\mathcal{G}}$ :  $\varepsilon^{\mathcal{G}}$ , the dissipating potential above takes the form

$$D = D_f \cdot \dot{\mathfrak{d}}_f + D_m \cdot \dot{\mathfrak{d}}_m \ge 0, \tag{39}$$

where  $\mathcal{D}_f$ , and  $\mathcal{D}_m$  are the forces associated with the fiber and the matrix, respectively, whose specific expression can be computed as

$$\mathcal{D}_{f} = 2(1 - \mathfrak{d}_{f})\Psi - G_{C,f} \left[ \frac{\mathfrak{d}_{f}}{\ell_{f}} - \ell_{f} \nabla \mathfrak{d}_{f} : \mathcal{A}_{f} : \nabla \mathfrak{d}_{f} \right], \tag{40}$$

$$D_{m} = g'(\mathfrak{d})\Psi - G_{C,m} \left[ \frac{\mathfrak{d}_{m}}{\ell_{m}} - \ell_{m} \nabla \mathfrak{d}_{m} : \mathcal{A}_{m} : \nabla \mathfrak{d}_{m} \right]. \tag{41}$$

Notice that, in order for the expression  $g'(\mathfrak{d})\Psi$  to be well defined, we consider  $\min(g_f,g_m)$  first and then consider the derivative of the  $g(\mathfrak{d})$ . Consequently, from Eq. (39), (40), and (41), along with the boundedness of the phase-field variables  $\mathfrak{d}_f,\mathfrak{d}_m\in[0,1]$  leads to the first order optimality conditions, referred to as Karush–Kuhn–Tucker (KKT) conditions. The particular form of the KKT conditions can be written as

$$\dot{\mathfrak{d}}_f \ge 0, -\mathcal{D}_f \le 0, \dot{\mathfrak{d}}_f \cdot \mathcal{D}_f = 0, \tag{42}$$

$$\dot{\mathfrak{d}}_m \ge 0, -\mathcal{D}_m \le 0, \dot{\mathfrak{d}}_m \cdot \mathcal{D}_m = 0. \tag{43}$$

Furthermore, in Eq. (40), and (41), the expression  $G_{C,i}\left[\frac{\mathfrak{d}_i}{\ell_i}-\ell_i\nabla\mathfrak{d}_i:\mathcal{A}_i:\nabla\mathfrak{d}_i\right]$  for each i=f,m indicates the energetic crack resistance, and  $g'(\mathfrak{d})\Psi(\varepsilon)$  is the crack driving force.

In order to enforce the irreversibility of the phase-field variables, the driving force based on the Puck Failure criteria is considered. Assuming the energy required for initiating the Puck failure is known as in Eq.

(35), and (36), the driving force takes the form

$$\mathcal{H}_{f} = \max_{\tau \in [0,T]} \left\{ \zeta_{f} \left( \frac{\Psi_{f}}{\Psi_{f,0}} - 1 \right) \right\} \quad \text{if} \quad \Psi_{f,0} > 0, \text{ and} \quad 0 \quad \text{otherwise},$$

$$\tag{44}$$

$$\mathcal{H}_{m} = \max_{\tau \in [0,T]} \left\{ \zeta_{m} \left( \frac{\Psi_{m}}{\Psi_{m,0}} - 1 \right) \right\} \quad \text{if} \quad \Psi_{m,0} > 0, \text{ and} \quad 0 \quad \text{otherwise.}$$
(45)

Here, the factors  $\zeta_f$ , and  $\zeta_m$  are the dimensionless parameters to characterize the activation of the fracture due to the fiber and matrix failure.

#### 5. Finite element implementation: Compact UEL

With this at hand, the solution to Eq. (22) at every discrete time step  $\tau \in [0,t]$  can be obtained by solving as a minimization problem. i.e., Determine  $(\mathbf{u},\mathfrak{d}_f,\mathfrak{d}_m)$  from

$$(\mathbf{u}^*, \mathfrak{d}_f^*, \mathfrak{d}_m^*) = \operatorname{Arg} \, \min_{S} \Psi(\mathbf{u}, \mathfrak{d}_f, \mathfrak{d}_m), \tag{46}$$

with  $S = \{\delta_f, \delta_m \geq 0, \text{ for all } \mathbf{x} \in \mathcal{B}\}$ . The triplet  $(\mathbf{u}, \delta_f, \delta_m)$  in Eq. (22) is solved by taking the first variation of the total energy functional. For any admissible test function  $(\delta \mathbf{u}, \delta \delta_f, \delta \delta_m)$  in an appropriate space of distributions, the following weak form for the continuous multi-phase field problem can be derived

$$\int_{B} \tilde{\sigma}^{G} : \epsilon^{G}(\delta \mathbf{u}) d\mathbf{x} - \int_{B} f_{v} \cdot \delta \mathbf{u} d\mathbf{x} + \int_{\partial B_{t}} \tilde{\mathbf{t}} \cdot \delta \mathbf{u} d\mathbf{S} = 0, (47)$$

$$\int_{B} G_{C,f} \left[ \frac{\mathfrak{d}_{f}}{\ell_{f}} \delta \mathfrak{d}_{f} + \ell_{f} \cdot \nabla \mathfrak{d}_{f} \cdot \mathcal{A}_{f} \cdot \nabla \delta \mathfrak{d}_{f} \right] d\mathbf{x} - \int_{B} \left( \tilde{\sigma}^{G} : \epsilon^{G} \delta \mathfrak{d}_{f} \right) d\mathbf{x} = 0, (48)$$

$$\int_{B} G_{C,m} \left[ \frac{\mathfrak{d}_{m}}{\ell_{m}} \delta \mathfrak{d}_{m} + \ell_{m} \cdot \nabla \mathfrak{d}_{m} \cdot \mathcal{A}_{m} \cdot \nabla \delta \mathfrak{d}_{m} \right] d\mathbf{x} - \int_{B} \left( \tilde{\sigma}^{G} : \epsilon^{G} \delta \mathfrak{d}_{m} \right) d\mathbf{x} = 0. (49)$$

The functional space  $\mathcal{B}$  is discretized into  $n_e$  non-overlapping isoparametric elements such that  $\mathcal{B} \approx \bigcup_{e=1}^{n_e} \mathcal{B}^{(e)}$  and partition of unity holds. Recalling the standard Bubnov–Galerkin methods, the functional space for the primary fields is defined as  $(\mathbf{u}, \mathfrak{d}_f, \mathfrak{d}_m) \in (\mathfrak{B}_u, \mathfrak{B}_f, \mathfrak{B}_m)$ . Where

$$\mathbf{u} \in \mathfrak{B}_{u} := \{ \mathbf{u} \in H^{1}(\mathcal{B}) | \nabla \mathbf{u} = \bar{u} \text{ on } \partial \mathcal{B}_{u} \}, \tag{50}$$

$$\mathfrak{d}_f \in \mathfrak{B}_f := {\mathfrak{d}_f \in H^1(\mathcal{B}) | \mathfrak{d}_f \in [0,1], \dot{\mathfrak{d}}_f \ge 0, \text{ for all } \mathbf{x} \in \mathcal{B}},$$

$$\mathfrak{d}_m \in \mathfrak{B}_m := \{\mathfrak{d}_m \in H^1(\mathcal{B}) | \mathfrak{d}_m \in [0,1], \dot{\mathfrak{d}}_m \ge 0, \text{ for all } \mathbf{x} \in \mathcal{B}\}. \tag{52}$$

Similarly, the test functions are defined in the functional spaces as  $(\delta \mathbf{u}, \delta \mathfrak{d}_f, \delta \mathfrak{d}_m) \in (\mathfrak{A}_u, \mathfrak{A}_f, \mathfrak{A}_m)$ . In specific,

$$\delta \mathbf{u} \in \mathfrak{A}_{m} := \{ \delta \mathbf{u} \in H^{1}(\mathcal{B}) | \nabla \delta \mathbf{u} = 0 \text{ on } \partial \mathcal{B}_{m} \}. \tag{53}$$

$$\delta \mathfrak{d}_f \in \mathfrak{A}_f := \{ \delta \mathfrak{d}_f \in H^1(\mathcal{B}) | \nabla \delta \mathfrak{d}_f \ge 0, \text{ for all } \mathbf{x} \in \mathcal{B} \}, \tag{54}$$

$$\delta \mathfrak{d}_m \in \mathfrak{A}_m := \{ \delta \mathfrak{d}_m \in H^1(\mathcal{B}) | \nabla \delta \mathfrak{d}_m \ge 0 \text{ for all } \mathbf{x} \in \mathcal{B} \}.$$
 (55)

With this setting, the primary fields and their respective gradients can be interpolated as

$$\mathbf{u}^e = \sum_{i=1}^{n_e} \mathbf{N}_i^u \mathbf{u}_i^e, \quad \delta_f^e = \sum_{i=1}^{n_e} \mathbf{N}_i^\delta \delta_{f,i}^e, \quad \delta_m^e = \sum_{i=1}^{n_e} \mathbf{N}_i^\delta \delta_{m,i}^e,$$
 (56)

$$\nabla \mathbf{u}^e = \sum_{i=1}^{n_e} \mathbf{B}_i^u \mathbf{u}_i^e, \quad \nabla \mathfrak{d}_f^e = \sum_{i=1}^{n_e} \mathbf{B}_i^{\mathfrak{d}} \mathfrak{d}_{f,i}^e, \quad \nabla \mathfrak{d}_m^e = \sum_{i=1}^{n_e} \mathbf{B}_i^{\mathfrak{d}} \mathfrak{d}_{m,i}^e,$$
 (57)

where  $\mathbf{N}_i^u$ , and  $\mathbf{N}_i^0$  are the shape functions associated with the node i for the fields  $\mathbf{u}$ , and two phase fields  $(\mathfrak{d}_f, \mathfrak{d}_m)$  respectively. Furthermore,  $\mathbf{B}_i^u$ , and  $\mathbf{B}_i^0$  are the derivatives of the shape functions at the node i for  $\mathbf{u}$ , and the two phase fields respectively. With the same interpolation functions for the variational test functions counterparts, i.e.,  $(\delta \mathbf{u}, \delta \mathfrak{d}_f, \delta \mathfrak{d}_m)$ , the discrete version of the elemental residual vectors takes the form

$$\mathbf{R}_{\mathbf{u}}^{e} = \int_{\mathcal{B}^{(e)}} (\mathbf{B}^{u})^{T} \tilde{\sigma}^{\mathcal{G}} d\mathbf{x} - \int_{\mathcal{B}^{(e)}} (\mathbf{N}^{u})^{T} \mathbf{f}_{v} d\mathbf{x} - \int_{\partial \mathbf{R}^{(e)}} (\mathbf{N}^{u})^{T} \bar{\mathbf{t}} d\mathbf{S}, \tag{58}$$

$$\mathbf{R}_{f}^{e} = \int_{B^{(e)}} -2(1 - \mathfrak{d}_{f})(\mathbf{N}^{\mathfrak{d}})^{T} \mathcal{H}_{f} + \frac{G_{C,f}}{\ell_{f}} \left[ (\mathbf{N}^{\mathfrak{d}})^{T} \mathfrak{d}_{f} + \ell_{f}^{2} (\mathbf{B}^{\mathfrak{d}})^{T} \mathcal{A}_{f} \nabla \mathfrak{d}_{f} \right] d\mathbf{x},$$
(59)

$$\mathbf{R}_{m}^{e} = \int_{\mathcal{B}^{(e)}} -2(1 - \mathfrak{d}_{m})(\mathbf{N}^{\mathfrak{d}})^{T} \mathcal{H}_{m} + \frac{G_{C,m}}{\ell_{m}} \left[ (\mathbf{N}^{\mathfrak{d}})^{T} \mathfrak{d}_{m} + \ell_{m}^{2} (\mathbf{B}^{\mathfrak{d}})^{T} \mathcal{A}_{m} \nabla \mathfrak{d}_{m} \right] d\mathbf{x}.$$
(60)

Notice that the system of equations is non-linear due to the presence of fracture and the Puck failure criteria embedded in the history variables  $\mathcal{H}_f, \mathcal{H}_m$ . From Eq. (59), (60), it is easy to see that the residuals corresponding to the fiber and the matrix failure are independent from each other but are coupled with the equilibrium equation (strain energy of the bulk) in Eq. (58). The corresponding Newton–Raphson iteration for the globally assembled system at (n+1) step can be expressed as

$$\begin{bmatrix} \mathbf{u} \\ \mathbf{d}_{f} \\ \mathbf{d}_{m} \end{bmatrix}_{n+1} = \begin{bmatrix} \mathbf{u} \\ \mathbf{d}_{f} \\ \mathbf{d}_{m} \end{bmatrix}_{n} - \begin{bmatrix} K^{\mathbf{u}\mathbf{u}} & 0 & 0 \\ 0 & K^{ff} & 0 \\ 0 & 0 & K^{mm} \end{bmatrix}_{n+1}^{-1} \begin{bmatrix} \mathbf{R}_{\mathbf{u}} \\ \mathbf{R}_{f} \\ \mathbf{R}_{m} \end{bmatrix}_{n}, \tag{61}$$

where the particular form of the elemental stiffness matrix reads

$$K^{\mathbf{u}\mathbf{u}} := \frac{\partial \mathcal{R}_{\mathbf{u}}^{e}}{\partial \mathbf{u}^{e}} = \int_{B^{(e)}} (\mathbf{B}^{u})^{T} \tilde{\mathbb{C}}_{\mathcal{C}} \mathbf{B}^{u} d\mathbf{x}, \tag{62}$$

$$K^{ff} := \frac{\partial \mathcal{R}_f^e}{\partial \mathfrak{d}_f^e} = \int_{\mathcal{B}^{(e)}} \left( 2\mathcal{H}_f + \frac{G_{C,f}}{\ell_f} \right) (\mathbf{N}^{\mathfrak{d}})^T \mathbf{N}^{\mathfrak{d}} + G_{C,f} \ell_f (\mathbf{B}^{\mathfrak{d}})^T \mathcal{A}_f \mathbf{B}^{\mathfrak{d}} d\mathbf{x},$$
(63)

$$K^{mm} := \frac{\partial \mathcal{R}_{m}^{e}}{\partial \mathfrak{d}_{m}^{e}} = \int_{\mathcal{B}^{(e)}} \left( 2\mathcal{H}_{m} + \frac{G_{C,m}}{\ell_{m}} \right) (\mathbf{N}^{\mathfrak{d}})^{T} \mathbf{N}^{\mathfrak{d}} + G_{C,m} \ell_{m} (\mathbf{B}^{\mathfrak{d}})^{T} \mathcal{A}_{m} \mathbf{B}^{\mathfrak{d}} \mathbf{d} \mathbf{x}.$$

$$(64)$$

The above system of equations has been implemented in Abaqus-UEL to take advantage of the in-built Newton–Raphson solver and the automatic time-stepping scheme. A detailed algorithm implementation is provided in Algorithm 1. The details regarding the codes, input files, are provided in the Data Availability section.

#### 6. Numerical examples

(51)

This section presents the performance of the proposed multi-phase field formulation. In this section, numerical examples concerning (i) Single-Edge Notched Tension (SENT), (ii) Open Hole Tension (OHT), (iii) Compact Tension (CT), (iv) Centre Notched Tension (CNT), (v) Three-Point Bending (TPB), (vi) Bi-Material Interface (BMI), and finally (vii) Tension in unnotched specimens are presented. Furthermore, this section is divided into two parts based on the nature of the examples concerning the literature. The first part, which includes benchmarks (i), (ii), (iii), and (iv), provides a comparison with the experimental results both qualitatively and quantitatively based on the crack propagation path and force reactions, respectively. The second part, with benchmarks (v), (vi), and (vii), are aimed to show the predictive capability of the proposed model. Furthermore, tension in unnotched specimens account for several possible defects, such as randomly distributed micro-cracks/impurities, to assess the crack propagation in tension without stress concentrators. With these examples, we aim to provide a list of cumulative benchmark examples for numerical applications. In each example, the fiber orientation is varied between 0° and 90° to understand the effects of the ply orientation, while the symmetric case such as  $-60^{\circ}$ ,  $-45^{\circ}$ , and  $-30^{\circ}$  are shown in Appendix

The material properties used for each example in the local ply coordinates are classified into four sections: (1) Elastic properties of the composite ply as in Table 1, (2) strength properties of the composite ply

**Table 1** Elastic properties of the composites.

E <sub>11</sub> (MPa)	E <sub>22</sub> (MPa)	E <sub>12</sub> (MPa)	$\nu_{11}$	$\nu_{23}$	G <sub>12</sub> (MPa)
114800	11700	9600	0.0222	0.21	9600

# **Table 2**Strength properties of the elastic.

$R_{11}^{T}$ (MPa)	$R_{22}^T$ (MPa)	$R_{11}^{C}$ (MPa)	$R_{22}^{C}$ (MPa)	R <sub>12</sub> (MPa)
2000	70	1650	240	105

Table 3

ruck failure properties.						
$P_{21}^{+}$	$P_{21}^{-}$	$P_{22}^{+}$	$P_{22}^{-}$	$E_{11}^F$ (MPa)	$v_{11}^F$	α
0.3	0.25	0.225	0.225	114800	0.21	0

Table 4
Multi-phase field properties.

$\ell_f$ [mm]	$\ell_m$ [mm]	$G_{C,f}\left[rac{ ext{N}}{ ext{mm}} ight]$	$G_{C,m}\left[rac{ ext{N}}{ ext{mm}} ight]$	$\zeta_f$	$\zeta_m$
0.1	0.3	106.3	0.7879	5	1

**Algorithm 1** Algorithmic implementation Multi-phase field model for FRGs with Puck failure Criteria.

**Input:** Given  $\{\mathbf{u}^n, \mathfrak{d}_f^n, \mathfrak{d}_m^n\}$ , compute  $\{\mathbf{u}^{(k),n+1}, \mathfrak{d}_f^{(k),n+1}, \mathfrak{d}_m^{(k),n+1}\}$ .

- 1. Compute Rotation Tensor  $\mathcal{R}$  according to Eq. (10).
- 2. Compute Structural Tensor  $A_f$ ,  $A_m$  according to Eq. (8).
- 3. Loop over the integration points based on the previous converged configuration  $t_n$
- 3.1 Compute the shape functions  $\mathbf{N}_{i}^{u}$ , and  $\mathbf{N}_{i}^{\delta}$  and the derivatives of the shape functions  $\mathbf{B}_{i}^{u}$ , and  $\mathbf{B}_{i}^{\delta}$ .
  - 3.2 Interpolate the nodal phase-field values.
- 3.3 Compute global strains with  $\epsilon_g = \mathbf{B}_i^u \cdot \mathbf{u}^n$ . and local strains using Eq. (11).
- 3.4 Construct the constitutive stiffness matrix in the local coordinate  $\mathbb{C}^{\mathcal{L}}$ , and compute the constitutive global stiffness matrix using Eq. (12).
- 3.5 Compute the stress in global coordinates using Eq. (13), and in local ply coordinates using Eq. (14).
- 3.6 Using  $\sigma^{\mathcal{L}}$ , compute the Puck exposure factors as in Section 3.
- 3.7 Compute the energy from fiber using Eq. (15), and energy from matrix using Eq. (17).
  - 3.8 Compute the driving forces using Eqs. (40) and (41).
- 3.9 Compute the degraded stiffness matrix and the stress using Eqs. (26) and (27) respectively.
- $3.10\ Pull$  back the degraded stress into the global system using Eq. (27).
- 3.11 Compute the residuals as in Eqs. (58)–(60), and stiffness matrix using Eqs. (62)–(64).
- 4. Construct the element matrices and the internal force vectors of the complete system.
- 5. Perform the final assembly.

as in Table 2, (3) Puck failure properties as in Table 3, and (4) Multiphase field properties as in Table 4. Specific material properties for each example are provided in the sequel. Additionally, unless otherwise noted, an approximate median value is provided together with the measurement error of  $\pm 0.2^{\circ}$  in order to quantify the crack propagation angles resulting from the numerical simulations.

## 6.1. Single Edged Notched Tension (SENT)

A single-edged notched tension specimen is considered in this sec-

tion to compare the crack propagation with the experimental investigation. The experimental results are taken from [76] and reproduced with permission from Elsevier. The example consists of the plate of dimension  $1\times 2$  mm with an edge notch, with fibers oriented at an angle  $\theta$  with respect to the global x-axis as shown in Fig. 3(a). The thickness of the specimen is taken as 1 mm. The bottom of the plate is fixed in y-direction, with one point fully restrained. The displacement load is applied on the top surface as shown in Fig. 3(a). No restriction is applied to the displacement in the horizontal direction at the top of the specimen. The numerical simulations compare the crack propagation path and the load reaction for different angled ply varying from  $0^{\circ}$  to  $90^{\circ}$ . The material properties are considered as in Tables 1–4 in line with the experimental results in [76].

The numerical experiments regarding the SENT specimen are also presented in [2-4,69,77] using the phase-field method. Fig. 4 presents the comparison of the crack path observed in the experiments and the present model for the fiber orientations  $\theta = 0^{\circ} - 60^{\circ}$ . The crack runs parallel to the fibers, leading to a matrix-dominated cracking. Furthermore, all the cracks grow in an unstable manner. The numerical results presented are in good agreement with the experimental observations. The Force vs. displacement graph for the fiber orientation of  $\theta = 0^{\circ} - 60^{\circ}$  is presented in Fig. 3 (b) along with the Puck initiation. The comparison between the present model and the other available models in the related literature is presented in Table 5. The crack propagation angles presented in the Table 5 are measured from the center, where the Phase-field value is dense in an undeformed configuration. The Table 5 shows an excellent agreement with the experimental methods compared to other models. Furthermore, Fig. C.26 presents the crack propagation for fiber oriented with  $\theta = -30^{\circ}$ ,  $\theta = -45^{\circ}$ , and  $\theta =$  $-60^{\circ}$ . Force vs. displacement results for the negative fiber orientation coincide with their positive counterpart. Hence, they are omitted for the sake of brevity.

Prior studies using phase-field literature, as in [2,69], reported that the fiber orientations  $\theta=90^\circ$  that involve fiber debonding are proven challenging due to the sharp turn and likelihood of the crack propagating both upward and downwards in the fiber direction. Consequently, the numerical crack propagation path in the related literature showed a deviation of  $3^\circ-8^\circ$  from the experimentally observed results. See Table 5. The results obtained from the proposed model for  $\theta=90^\circ$  are presented in Fig. 5(b). It can be seen that the numerical model accurately describes the experimental results even for the fiber oriented at  $\theta=90^\circ$ . The Force vs. displacement graph for the  $\theta=90^\circ$  is presented in Fig. 5(a) along with the force at which Puck failure initiates. In all the SENT examples, it is observed that a long nucleation phase follows Puck

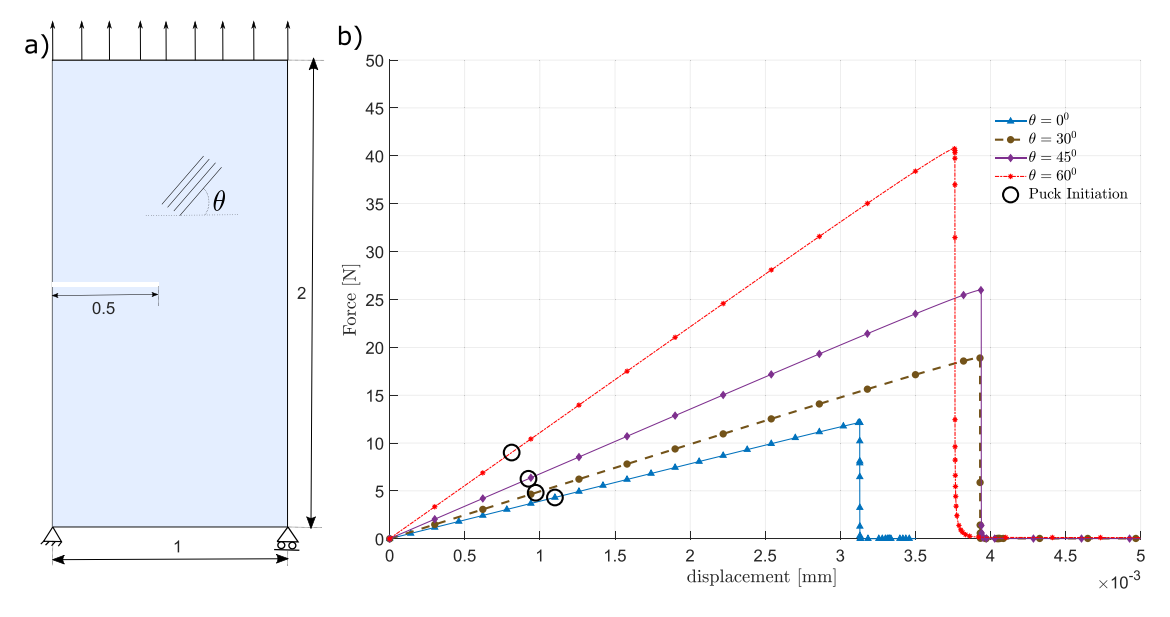


Fig. 3. (a) Geometric description of the single-edged notched tension specimen (all the units are in mm), (b) force vs. displacement plots along with Puck initiation for the fiber orientations of  $0^{\circ}$ ,  $30^{\circ}$ ,  $45^{\circ}$ , and  $60^{\circ}$ .

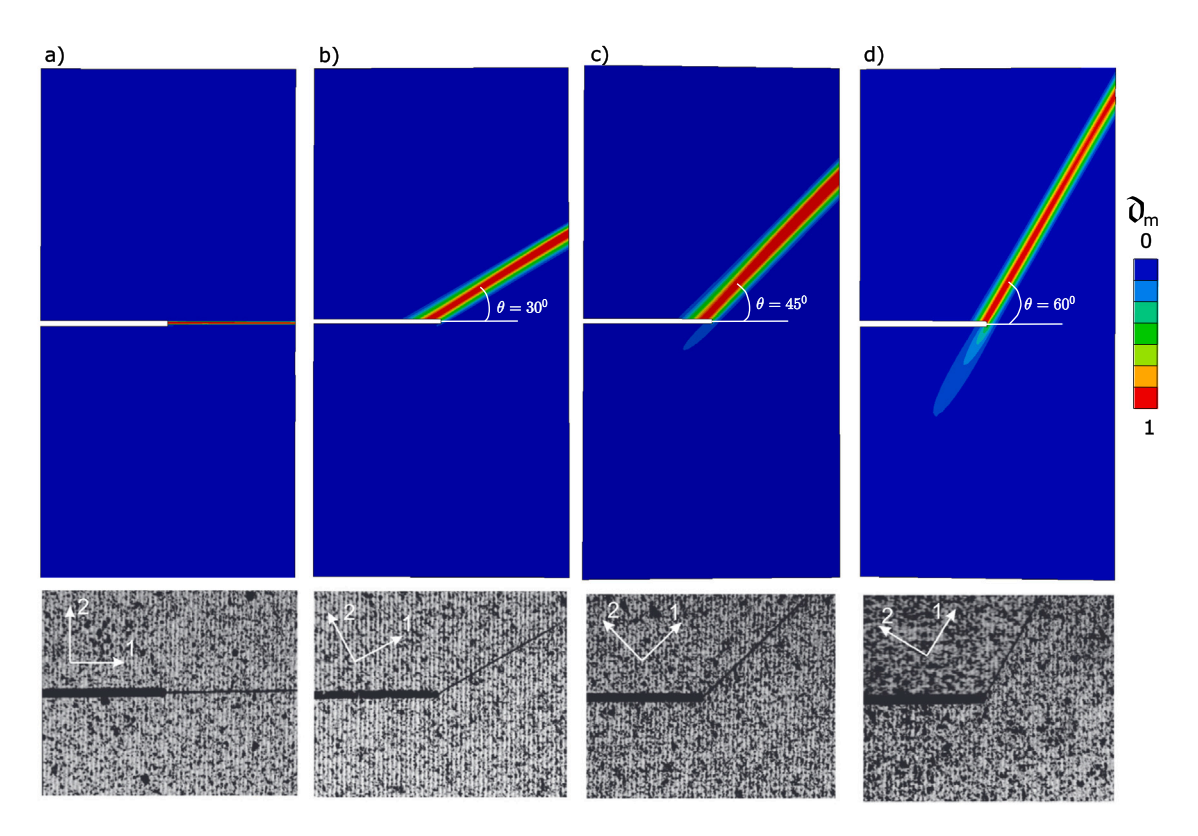


Fig. 4. Comparison between experimental results from [76] and the present model in terms of crack propagation for the fiber orientations of (a)  $\theta = 0^{\circ}$ , (b)  $\theta = 30^{\circ}$ , (c)  $\theta = 45^{\circ}$ , and (d)  $\theta = 60^{\circ}$ . Results from [76] are reproduced with permission from Elsevier.

failure initiation before the crack propagation and subsequent drop in the reaction force.

## 6.2. Open-hole tension

The second example aims to show the responses to an open-hole tension. The experimental results for the open hole tension are taken from [78]. The experimental results are presented for the fiber orientations of  $\theta=0^\circ$ ,  $\theta=45^\circ$ , and for  $\theta=90^\circ$  whose dimensions differ across

each specimen subjected to fiber orientation. Consequently, this section is divided into two parts: (a) Comparison with the experiment based on [78] and (b) generalized numerical results. In order to compare the experimental investigation in terms of crack propagation path and the load response, section (a) is provided. After establishing the comparison with experimental results, a generalized results are presented with the same geometry across all the fiber orientations to effectively understand the effect of the fiber orientation.

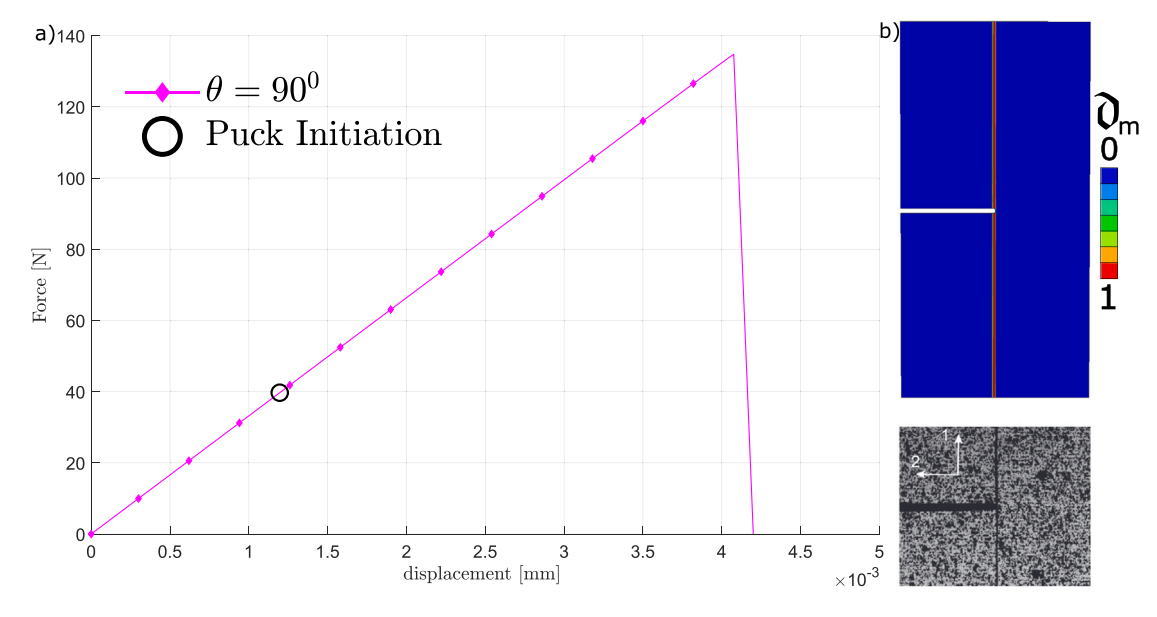


Fig. 5. (a) Force vs. displacement plot along with the Puck failure initiation for fiber orientation of 90°. (b) Comparison of crack propagation between experimental results from [76] and the present model. Results from [76] are reproduced with permission from Elsevier.

Table 5
Comparison between the present and the other available methods.

Fiber orientation	0°	30°	45°	60°	90°
Experimental results [76]	0	30	45	60	90
Cahill et al. [76] (XFEM)	0	29	43	57	83
Zhang et al. [2]	0	29	43.6	57.5	87
Ishank et al. [69]	0	28.2	42.5	56	85.4
Pranavi et al. [4]	_	29	42	55	_
Mrunmayee et al. [3]	_	27.3	42.7	57	_
Hrishikesh et al [77]	0	27.5	42	57	_
Present model	0	30.35	46.18	60.40	90

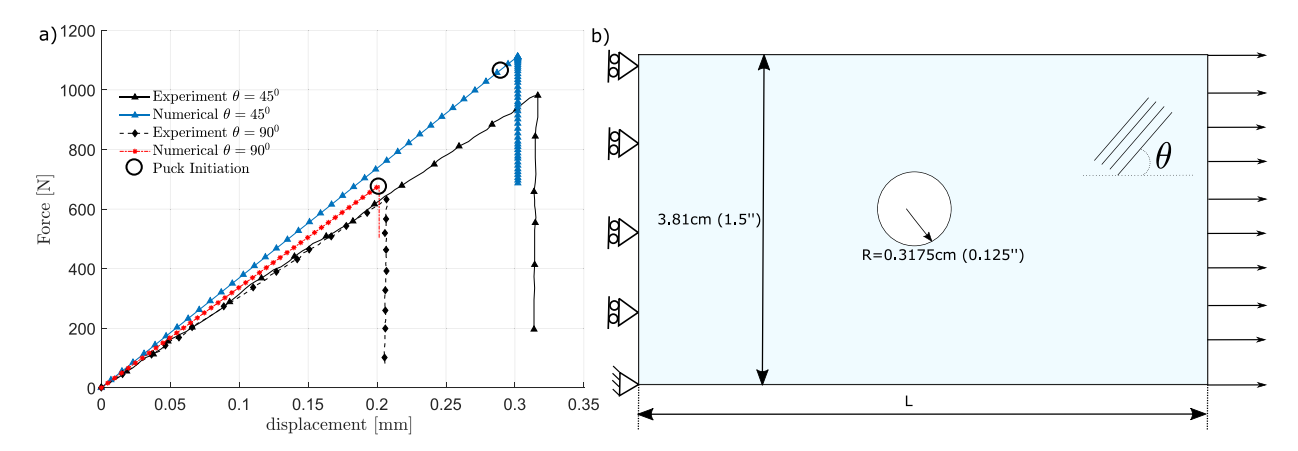
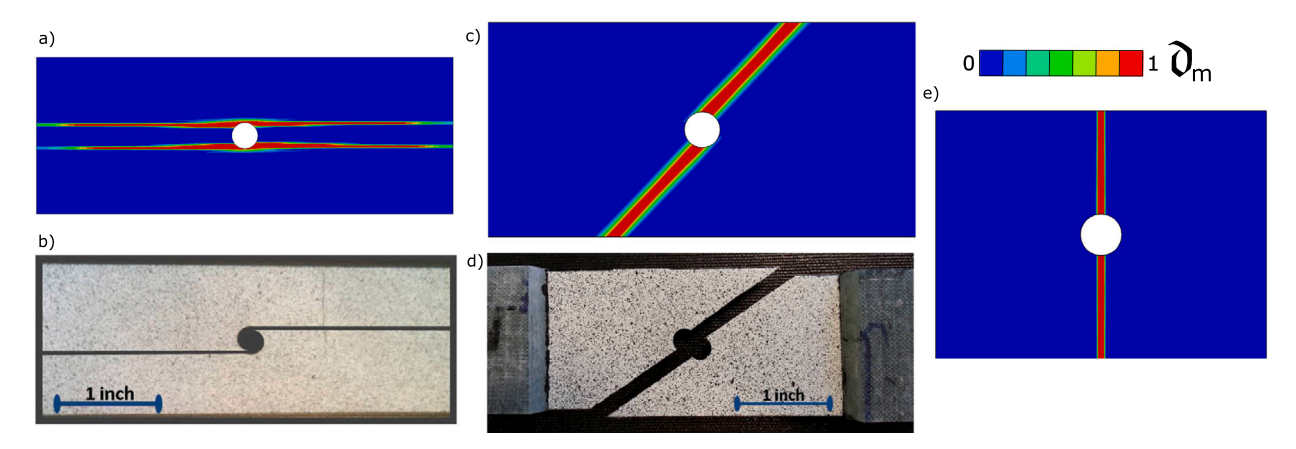


Fig. 6. (a) Force vs. displacement curve comparison for the open hole tension between the experiment [78] and the present model. (b) Geometrical description of the open hole tension specimen for comparison with the experiment.

## 6.2.1. Comparison with the experiments

The open hole tension has been addressed numerically using phase field method in [2,3,35,79–81]. Fig. 6(b) presents the geometrical description of the specimen. Furthermore, the width of the specimen is always kept constant at 3.81 cm (1.5 $\epsilon$  inch). The length L is taken as L=5.08cm (2 $\epsilon$  inch) for fiber orientation of  $\theta=90^\circ$ , L=7.62cm (3 $\epsilon$  inch) for  $\theta=45^\circ$ , and the L=10.16cm (4 $\epsilon$  inch) for  $\theta=0^\circ$  in line with the experiment [78]. The numerical simulations considers the elastic properties of the specimen to be  $E_{11}=136000$  MPa,  $E_{22}=4670$  MPa,  $E_{12}=G_{12}=3200$  MPa,  $v_{12}=0.011$ , and  $v_{23}=0.33$ . Meanwhile, the strength properties are taken as  $R_{11}^T=2142$  MPa,  $R_{22}^T=42.5$  MPa, and

 $R_{12}=90$  MPa. Furthermore, the fracture properties are considered as  $\ell_f=10$  mm, and  $\ell_m=6$  mm,  $G_{C,f}=81.5\frac{\rm N}{\rm mm}$ , and  $G_{C,m}=0.67\frac{\rm N}{\rm mm}$  in line with the experimental observations [78]. Fig. 6(a) compares force vs. displacement plots between the experimental results and the proposed model along with the Puck Initiation, while Fig. 7 compares the crack propagation path concerning the experimental observation. For the ply with the fiber orientation of  $\theta=45^\circ$ , the numerical results show a crack propagation angle of  $\theta=45.64^\circ\pm0.25^\circ$  in line with the experimental results. For the  $\theta=90^\circ$ , the experimental results are partially provided in [78] without the picture of the experimental observation; hence, only results stemming from the numerical results



**Fig. 7.** Comparison with the experiments for the open hole tension. Numerical results for (a)  $\theta = 0^{\circ}$  (c)  $\theta = 45^{\circ}$ , and (e)  $\theta = 90^{\circ}$ . The experimental results for the (b)  $\theta = 0^{\circ}$ , and (d)  $\theta = 45^{\circ}$ . The experimental results are produced from [78] with permission from Elsevier.

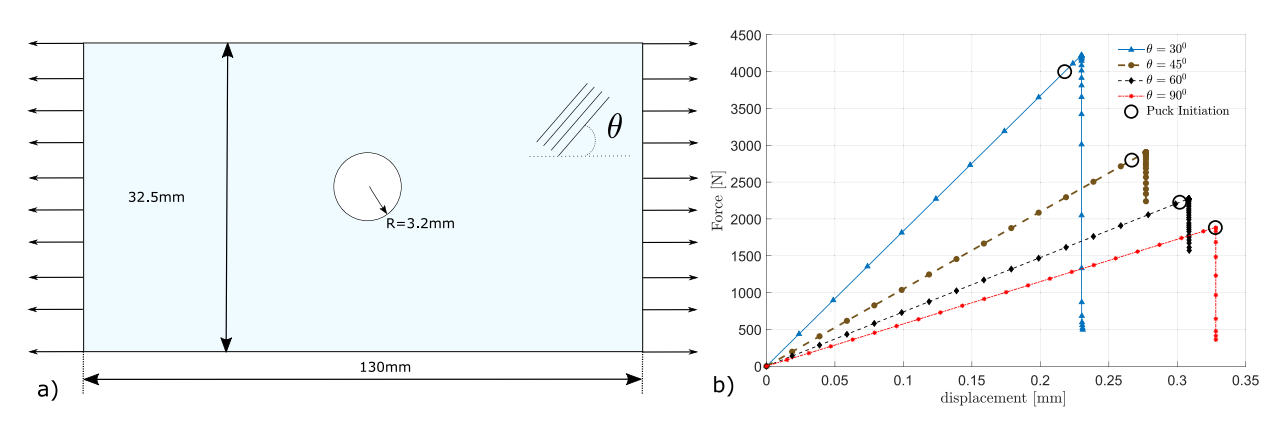


Fig. 8. Geometrical description of the open hole tension specimen. (b) Force vs. disp plots along with the Puck failure initiation for the fibers oriented at an angle of  $\theta = 30^{\circ}$ ,  $\theta = 45^{\circ}$ ,  $\theta = 60^{\circ}$ , and  $\theta = 90^{\circ}$ .

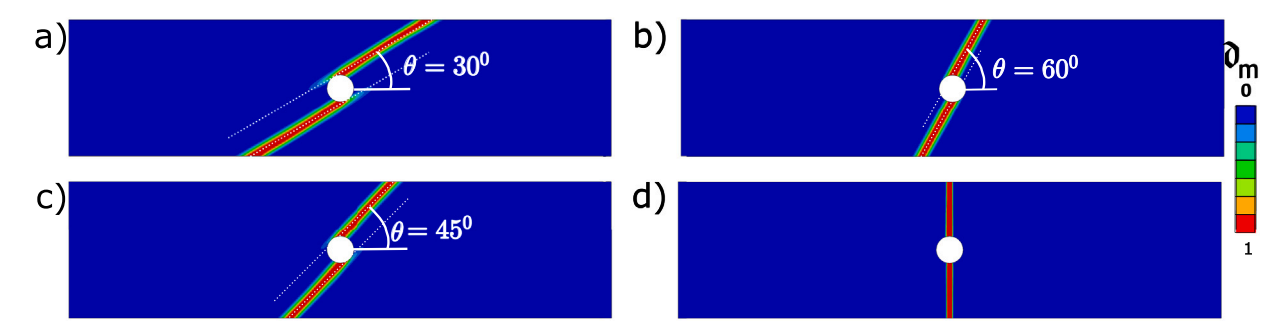


Fig. 9. Crack propagation in open hole tension for the fiber angles of (a)  $\theta = 30^{\circ}$ , (b)  $\theta = 60^{\circ}$ , (c)  $\theta = 45^{\circ}$ , (d)  $\theta = 90^{\circ}$ .

are presented. A similar pattern of crack propagation can also be seen in [79]. For the case with fibers orientated horizontally, i.e.,  $\theta=0^\circ$ , the crack propagation has an equal probability of propagating from both top and bottom part of the hole. Consequently, the numerical results show symmetrical crack propagation from both the top and bottom parts of the hole. In conclusion, the force vs. displacement presented in Fig. 6(b) and crack propagation path presented in Fig. 7 show excellent co-relation both qualitatively and quantitatively with the experimental observations.

## 6.2.2. Generalized open hole tension

In order to standardize the results from open-hole tension, a general geometry is used. The Fig. 8(a) shows the geometry under consid-

eration taken from [82]. A symmetric boundary condition consisting of a prescribed displacement along the x-coordinate on the left and right edges of the plate is applied. Within this context, eight different fiber directions are considered, i.e. fibers with orientation of  $0^{\circ}$ ,  $30^{\circ}$ ,  $45^{\circ}$ ,  $60^{\circ}$ ,  $90^{\circ}$ ,  $-30^{\circ}$ ,  $-45^{\circ}$ , and  $-60^{\circ}$ . The domain is discretized using 12712 4-node quadrilateral plane stress elements. Each of the numerical simulations considers the characteristic length scale of fiber and matrix as  $\ell_f = 8$  mm, and  $\ell_m = 4$  mm respectively, while the rest of the properties are kept as presented in Tables 1–3.

The crack propagation results stemming from the OHT for the fiber orientation of  $30^{\circ}$ ,  $45^{\circ}$ ,  $60^{\circ}$ , and  $90^{\circ}$  are shown in Fig. 9. Each of the figures also presents the principle material direction in a white dotted line along the crack propagation path. The actual crack propagation

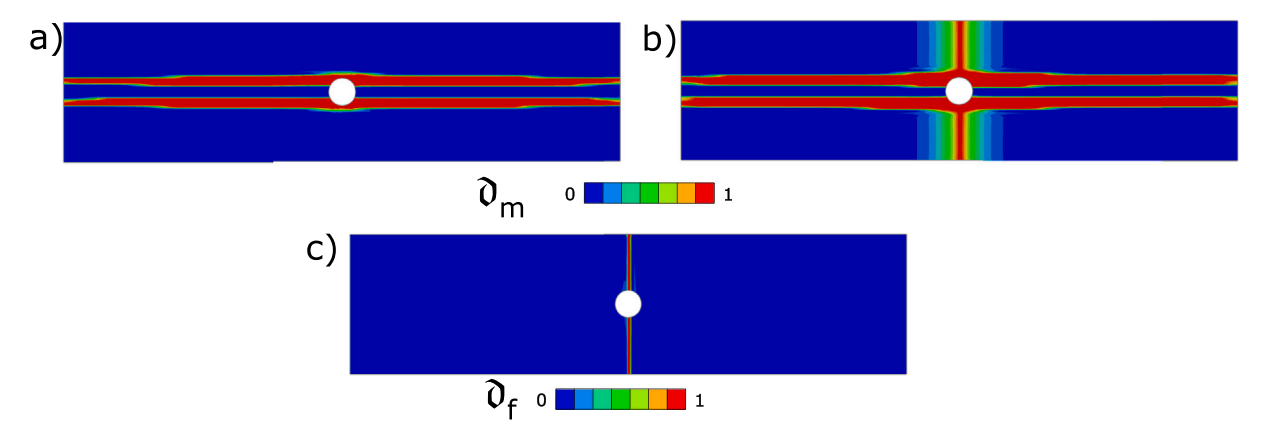


**Fig. 10.** Crack propagation in the open hole tension for the fiber orientation of  $\theta = 0^{\circ}$ .

angles for fiber orientations of  $30^\circ$ ,  $45^\circ$ ,  $60^\circ$  are measured to be  $31.2^\circ$ ,  $46.18^\circ$ ,  $60.56^\circ$  with an measuring error of  $\pm 0.2^\circ$ . Besides the case where the fibers coincide with the horizontal direction, all cases exhibit purely matrix-dominated cracking behavior, where only the matrix is damaged parallel to the fiber direction with no activation of fiber failure. The crack propagation in the symmetric case of  $-30^\circ$ ,  $-45^\circ$ , and  $-60^\circ$  are presented in Appendix Fig. D.27.

For the fiber orientation of  $0^{\circ}$ -case, the matrix-dominated failure occurs along the fiber direction, where the matrix crack stemming from the top and the bottom of the open hole extends as in Fig. 10(a). Furthermore, the matrix crack is accompanied by a fiber failure that runs across the specimens vertically, starting from the top and bottom of the hole, as in Fig. 10(c). Consequently, the matrix gets damaged in the areas where fiber failure is present, as in Fig. 10(b).

Due to the interaction between the fiber and inter-fiber failure, the behavior of the fibers with the orientation of 0° differs from the other cases. All cases except the 0°-exhibit unstable crack growth, indicated by the sharp drop in reaction force once the crack has formed. This can be observed from Fig. 8(b). Furthermore, the force vs. displacement curves exhibit a linear behavior until the Puck matrix failure initiation (independent of the PUCK mode) criteria are met, followed by an unstable crack growth and complete failure of the structure. Additionally, the displacement at failure of each structure decreases with the decreasing fiber orientation angle while the structure's loadbearing capacity increases. This could be attributed to the involvement of fiber at lower ply angles. It is also interesting to note that, as the fiber orientation changes from 90° to 30°, the delay between Puck failure initiation and unstable crack propagation increases. Precisely, for the fiber orientation of 90°, the puck failure initiation is immediately followed by unstable crack propagation, while for the fiber orientation of 30°, the Puck failure initiation is followed by a small nucleation phase before unstable crack propagation as shown in Fig. 8(b).

## 6.3. Compact tension

This example compares the experimental and numerical investigations regarding the crack propagation path in compact tension specimens subjected to tensile loading conditions. The experimental results presented in this section are mainly from the Institute of Polymer Product Engineering, Johannes Kepler University, Linz, Austria. The details regarding the experimental setup are omitted in this article. The geometry under consideration as in the experimental setup is presented in Fig. 11(a), with a thickness of 5.5 mm. A symmetric loading is applied to the top and bottom surface via the holes using the clamps as in Fig. 12(b) (for example). The experiment consists of carbon fiber reinforced unidirectional plies, each of thickness 0.125 mm, stacked on top of each other. Three different orientations of  $0^{\circ}$ ,  $45^{\circ}$  (considered as  $-45^{\circ}$  as per the previous numerical convention), and  $90^{\circ}$ . The crack

propagation path in the experiments for the fiber orientation of  $0^{\circ}$ ,  $45^{\circ}$  ( $-45^{\circ}$ ), and  $90^{\circ}$  are presented in Fig. 12(b), (d) and (f) respectively. It is also evident from Fig. 12 that the crack propagation follows the path of the fiber orientation. Consequently, this led to an inter-fiber-dominated failure. Similar experimental results regarding the compact tension for the fiber orientations of  $0^{\circ}$  and  $90^{\circ}$  can be found in [83].

The numerical results concerning the compact tension utilize the material properties as in Tables 1-4. Furthermore, the characteristic length scale associated with the matrix is considered as  $\ell_m = 2.5$  mm, while the length scale associated with fiber as  $\ell_f = 5$  mm. The numerical model is meshed with 36947 elements to map the structure accurately. The Fig. 11(a), (c) and (e) presents the comparison of the crack path for the fiber orientations of 0°, 45° (-45°), and 90° respectively. The crack propagation path obtained in the numerical results is measured as  $0^{\circ}$ ,  $45.40^{\circ} \pm 0.2^{\circ}$ , and  $90^{\circ}$  respectively. The results show the ability of the model to accurately describe the crack propagation path in comparison with the experiments. Furthermore, for the case with fiber orientations of 90°, the experimental results shows crack propagation upwards as in Fig. 12 (f), while the numerical results show the crack propagation in both upward and downward directions. This could be due to two main factors: (a) the asymmetrical notch due to machining arising from the experimental setup, and (b) the probability of the crack taking the path. The experimental results of the multiple samples show that the crack propagation is sometimes upward and sometimes downward. Consequently, due to geometrical symmetry, the numerical model predicts both the possibility of crack propagation in samples with fiber orientation of 90°. Furthermore, Fig. 13 presents the crack propagation for the fiber orientations with 30°, 45° and 60°. In all the cases, inter-fiber-dominated failure is observed. Fig. 11(b) presents the force vs. displacement curves for fiber orientations of 0°-90° along with the Puck Initiation. It can be easily observed that as the fiber orientation increases, the structure's load-bearing capacity increases. For the fiber orientations close to 90°, the strength of the structure increases, leading to more fracture resistance. Note that the force vs. displacement curves are not compared against the experimental work, and this will be presented in our future article along with the detailed experimental results. Additionally, the crack propagation in the symmetric cases is presented in Appendix Fig. E.28.

## 6.4. Centre Notched Tension (CNT)

This example shows the model's ability to predict crack propagation and compares them with the experimental results for the center-notched tension plate. The experimental results concerning the center-notch tension specimens are presented in [76]. The geometry, excluding the clamps for the mounting, consists of the Length of  $L=48~\mathrm{mm}$  and the width of  $W=25~\mathrm{mm}$ . The notch is placed at the center of the plate, and its width is considered to be 9.6 mm. Numerically, only

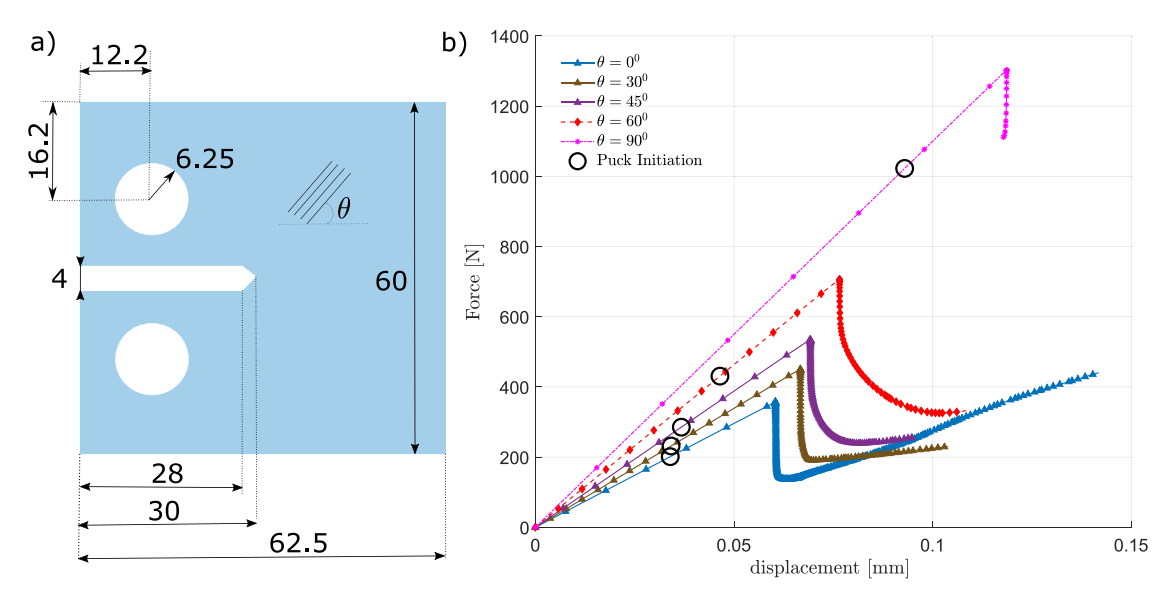


Fig. 11. (a) Geometrical description of the compact tension specimen under consideration, (b) force vs. displacement curve along with the Puck failure initiation for the fiber orientations of  $0^{\circ}$ ,  $30^{\circ}$ ,  $45^{\circ}$ ,  $60^{\circ}$ , and  $90^{\circ}$ .

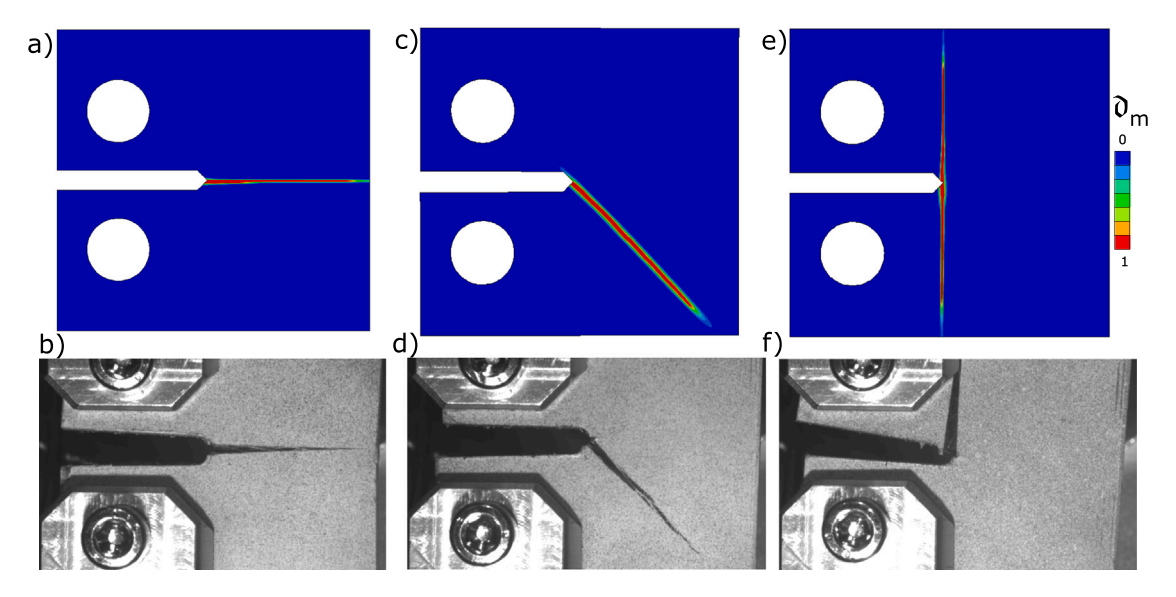


Fig. 12. Comparison between the experimental observation and present model of the crack propagation path in compact tension for fiber orientation of (a), (b) 0°, (c), (d) 45°, and (e), (f) 90°. Credits: Prof. Zoltán Major, Johannes Kepler University, Linz, Austria.

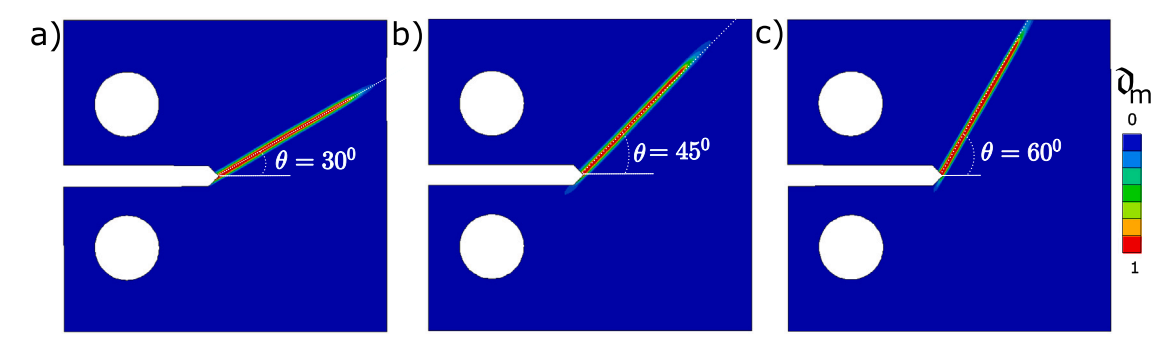


Fig. 13. Crack propagation in compact tension specimen for the fiber orientation of (a) 30°, (b) 45°, and (c) 60°.

the geometry without clamps is modeled with 15524 elements. The bottom part of the plate is completely fixed, where the displacement boundary conditions are applied to the top boundary. The material properties are taken as in Tables 1–4 in line with the experimental setup [76]. The characteristic length scales for the matrix and the fibers are considered as  $\ell_m=10$  mm and  $\ell_f=4$  mm. respectively. Fig.

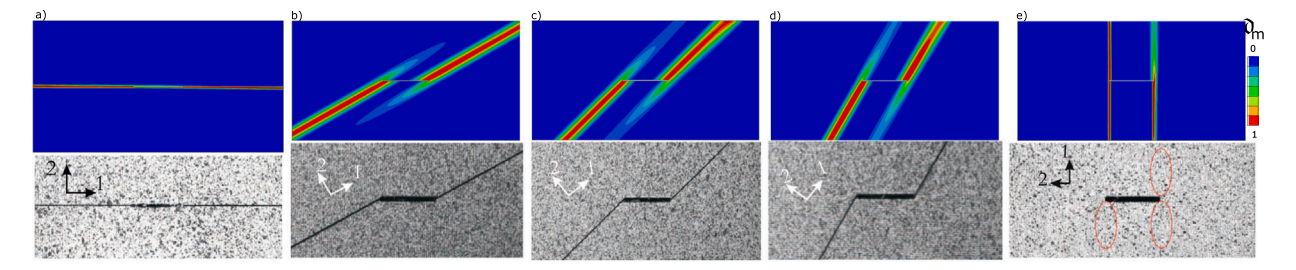


Fig. 14. Comparison between the experimental observations from [76] and the present model for the fiber orientations of (a)  $0^{\circ}$ , (b)  $30^{\circ}$ , (c)  $45^{\circ}$ , (d)  $60^{\circ}$ , and (e)  $90^{\circ}$ . The experimental results are reproduced from [76] with permission from Elsevier.

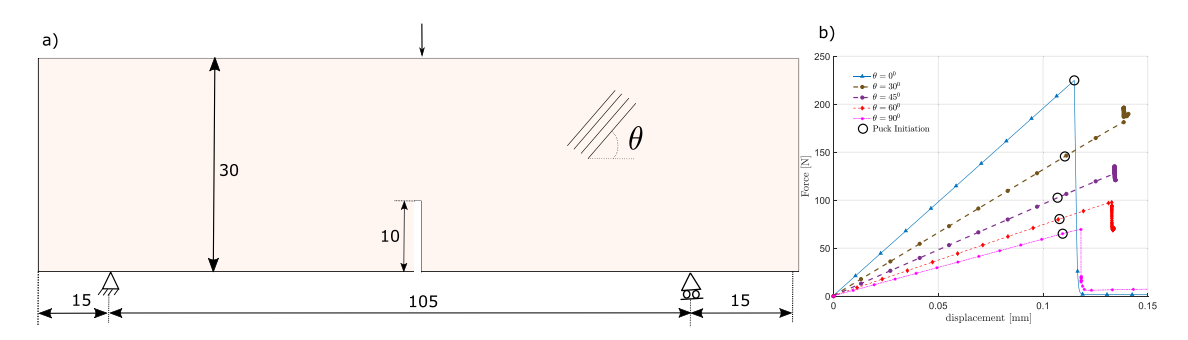


Fig. 15. (a) Geometrical description of the three point bending specimen. (b) Force vs. displacement curves along with the Puck failure initiation in TBP specimen for the fiber orientation of  $0^{\circ}$ ,  $30^{\circ}$ ,  $45^{\circ}$ ,  $60^{\circ}$ , and  $90^{\circ}$ .

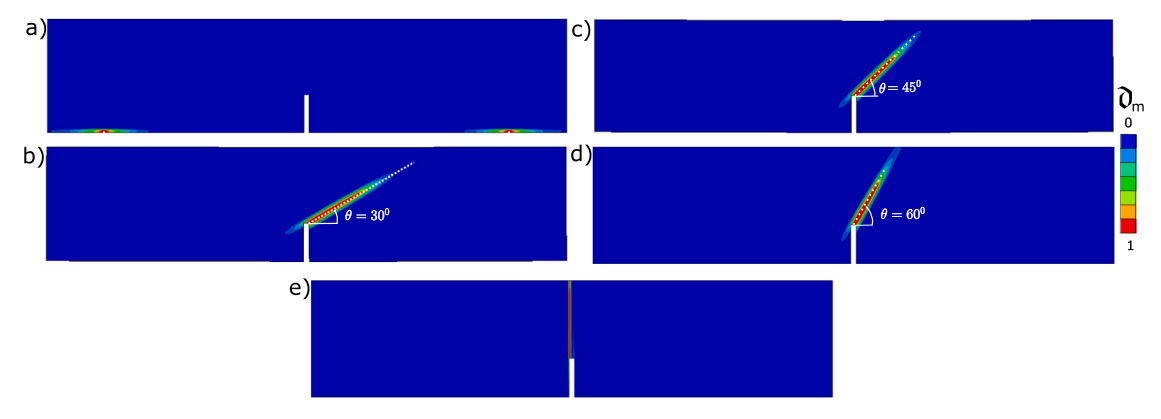


Fig. 16. Crack propagation in three-point bending specimen with fiber orientation of (a) 0°, (b) 30°, (c) 45°, (d) 60°, and (e) 90°.

14 presents the comparison of the crack path with the experimental observations for the plies with fiber orientations of 0°, 30°, 45°, 60°, and 90° in the same order as mentioned here. Furthermore, the actual angles of the crack prorogation from the numerical results are estimated as  $0^{\circ}$ ,  $29.85^{\circ} \pm 0.2^{\circ}$ ,  $44.52^{\circ} \pm 0.2^{\circ}$ ,  $59.85^{\circ} \pm 0.2^{\circ}$ , and  $90^{\circ}$  respectively. All the failure mechanisms are flagged as matrix-dominated failures. Consequently, the length scale corresponding to the fiber does not play any role. For the fiber with the orientations of 90°, experimental investigation as in Fig. 14(e) suggests that the likelihood of crack propagating from both sides is equal. Furthermore, the crack is likely to travel symmetrically up and down. Within this context, only one crack travels and reaches the top and bottom clamping surface due to crack shielding, while the other crack only propagates either top or bottom. The numerical observations presented in Fig. 14(e) also match the experimental observation [76]. Force vs. displacement curves are not given for the CNT specimens for brevity reasons. However, it has been observed that the force vs. displacement curve follows a similar pattern to that of SENT specimens.

## 6.5. Three-point bending

This section shows the crack propagation in a three-point bending specimen. The numerical simulations are done with the different fiber orientations as in Sections 6.1 and 6.2. All the numerical specimens use the same geometry and discretization as in the previous sections. The geometry consists of a unidirectional ply of length  $L=145\,$  mm with the span of  $S=105\,$  mm. A notch is placed at the center of the span with a one-third height of the specimen. Furthermore, the specimen has two supports, where the left support is a fixed and the right support is a floating bearing. The load is applied as a constant displacement at the top of the specimen as shown in Fig. 15(a). The domain is discretized with 20736 elements. The material properties are taken as in Tables 1–4 with  $\ell_m=4\,$  mm and  $\ell_f=8\,$  mm. A similar analysis for the three-point bending using phase field is shown in [84], where the authors consider stiff support for the effective distribution of the force.

In our numerical simulation, we observed that the supports fail, and no crack propagation is found for the case with fiber orientations of  $0^{\circ}$ . Fig. 16(a) shows the damage at the supports. Furthermore, for

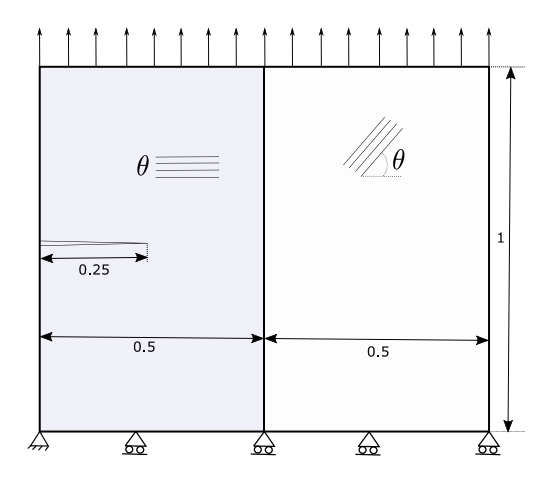


Fig. 17. Geometrical description of the bi-material interface specimen.

the fiber orientation of 30°, 45° crack propagation is shown in Fig. 16(b), (c) respectively are obtained. After these points, the crack is developed at load application points, leading to abrupt changes in the force vs. displacement plot. Consequently, only the results until this point are considered for the simulation. This could be due to the low matrix strength compared to the fibers. As a workaround, stiff boundaries can be considered as in [84]. Furthermore, Fig. 16(d) and (e) present the three-point bending for the fiber orientations of 60°, and 90°, respectively. No failed boundary issues are found in these cases. Fig. 15(b) presents the force vs. displacement curve for the three-point bending specimen for various fiber orientations along with their Puck initiation. As the angle of the fiber increases, the structure's load-bearing capacity increases, contrary to the other sections. This is due to the definition of the fiber orientation angle and the load application direction of the fiber orientation in the geometric description.

Furthermore, in order to simulate the crack propagation in the ply with fiber orientation of  $0^{\circ}$ , stiff sections are introduced at the boundaries as in Appendix Fig. G.30(a). The crack propagation due to the stiff boundaries is presented in Appendix Fig. G.30(d) with fiber orientation of  $0^{\circ}$ . The numerical simulations show that the crack forms horizontally as the load increases, leading to stable crack propagation until the crack propagates the whole structure span. Furthermore, stiff boundaries induce longer cracks for the fiber orientations of  $30^{\circ}$ ,  $45^{\circ}$  as shown in Fig. G.30.

## 6.6. Bimaterial interface

This section presents the model's predictive capability to handle interfaces between two different fiber orientations. For this purpose, a unit square with an edge notch is divided into two segments. A depiction of the problem, including its boundary condition, is shown in Fig. 17. The left segment is always set up to have a fiber orientation of 0°, while the right side has different fiber directions for each case, as in [4]. These fiber directions are 30°, 45°, 60°, and 90°. The same discretization and boundary conditions are used for each case, with the domain being discretized by 20306 elements. The material properties are different to the ones in Tables 1-2 with the elastic properties being  $E_{11}=171000$  MPa,  $E_{22}=9080$  MPa,  $G_{12}=5390$  MPa and  $v_{12}=0.0169$ . The strength properties are set to  $R_{11}^T=2323.5$  MPa,  $R_{22}^T=62.3$  MPa,  $R_{11}^C=1200.1$  MPa,  $R_{22}^C=199.8$  MPa and  $R_{12}=92.3$  MPa. The properties relating to Puck failure are the same as in Table 3. Lastly, the multiphase field properties are considered to be  $\ell_f=0.1$  mm,  $\ell_m=0.05$  mm,  $G_{C,f}=81.5~\frac{\rm N}{\rm mm}$  and  $G_{C,m}=1.2774~\frac{\rm N}{\rm mm}$  while the rest of the properties remain unchanged. A similar example for the bi-material interface and multiple interface problems has been presented in [4], where a traction separation law is used at the interface to differentiate the layers. This

article shows that the presented model can be used directly without any cohesive zone model. Within the context of [4], the work in this article presents a perfect interface. In contrast, the soft interfaces need an additional layer between the left and right domains with reduced stiffness (and fracture toughness).

The matrix damage plots for all cases except 90° are shown in Fig. 18. All cases exhibit a matrix crack along the different fiber orientation, showing that the present implementation can handle material interfaces. Furthermore, when the crack hits the interface, a small kinking of the crack in the left interface can be seen before the crack propagates on the right domain. This could be due to the bonded interface leading to a change of material properties at the interface. Similar kinking can also be observed in [4]. For the fiber orientations corresponding to 90°, the interaction between the matrix damage and fiber damage can be clearly seen in Fig. 19. Within this context, first, the matrix fails in the left domain and propagates to the interface. As soon as the crack hits the interface, the crack starts to propagate upwards, following the fiber direction of the right domain as presented in Fig. 19(a) leading to a classic example of debonding along the fiber-matrix interface. Furthermore, fiber damage is initiated at this point but not fully damaged; consequently, fibers in tension can be seen in Fig. 19(b). As the crack progresses, the crack arrests while increasing the fiber tension as shown in Fig. 19(c) and (d).

Fig. 20 shows the force–displacement curves for fiber orientations of 30°, 45°, and 60°. All cases exhibit linear elastic behavior at first, followed by a sudden drop in the reactions as soon as the crack hits the interface. For each case, a color-coded map of the crack hitting the interface and the corresponding load drop in the force vs. displacement is presented in Fig. 20. The cases with fiber orientations of 45° and 60° exhibit higher stiffness given the loading direction, leading to stable crack propagation in the beginning and becoming unstable when the crack is close to the boundary. Furthermore, the fibers with orientations of  $\pm 30^\circ$  show completely unstable crack propagation, leading to a further drop in the force as shown in Fig. 20.

## 6.7. Tension in unnotched specimens

Carbon Fiber-Reinforced Polymers (CFRPs) are prone to defects. The defined variability from the nominal flat laminate is often classified as a defect. See [85] for more details. The fiber defects can occur due to misalignments, in-plane and out-of-plane fiber undulations, and folds of the plies in fiber or transverse to fiber directions. Furthermore, the fiber defects depend highly on the fiber architecture [85]. At the same time, matrix defects stem from porosity or starved areas, dry spots, and fiber washouts [86]. The studies regarding the defects suggest a reduction of 10% in the strength due to the fold defects [87–89]. The effects of the voids, fiber washouts, and the locally compacted regions can be found in [90,91] and the reference therein.

Consequently, this example aims to show the intricate nature of the crack propagation in the specimens without any stress concentrations. Under these conditions, the crack first initiates microscopically, followed by a coalescence. These cracks nucleate, combine to form a larger crack followed by propagation. Under such circumstances, the crack path can only be entirely determined if the statistical data regarding the internal flaws of the structure is available. In order to solve such a system numerically, a few randomly distributed cracks are installed in the structure by reducing the fracture energy (or strength) at those points by 5%–10% herein refereed to as defect points. Furthermore, due to the reduced fracture energy (or strength), micro-cracks are formed at these points, followed by a coalescence and crack propagation.

Fig. 21(a) presents the geometrical description of the specimen. A pristine plate with fibers oriented in  $0^{\circ}$  and  $90^{\circ}$  is used for this example. For the ply with fiber orientation of  $30^{\circ}$ ,  $45^{\circ}$ , and  $60^{\circ}$  the geometry in Fig. 21(a) would always have a crack starting from the boundary. To circumvent the boundary effects in the angles plies, another geometry with a length of L=5 mm is taken. In order to simulate the actual test

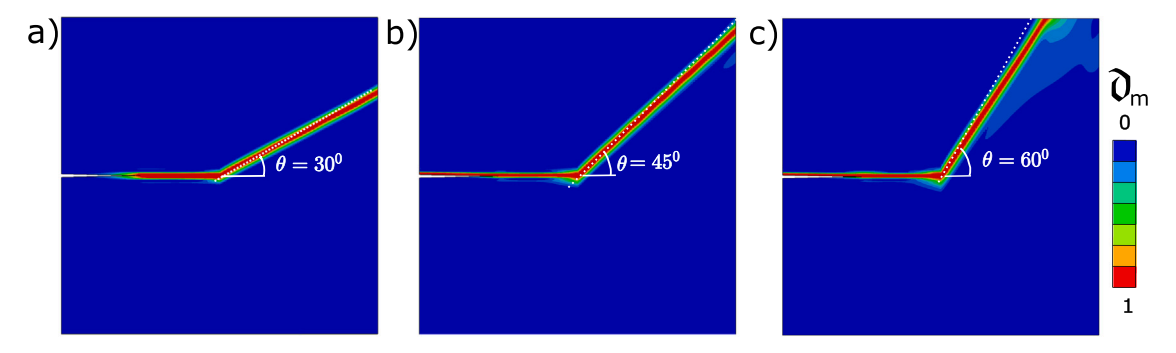


Fig. 18. Crack propagation in the bi-material interface for the fiber orientation of second layer of (a) 30°, (b) 45°, and (c) 90°.

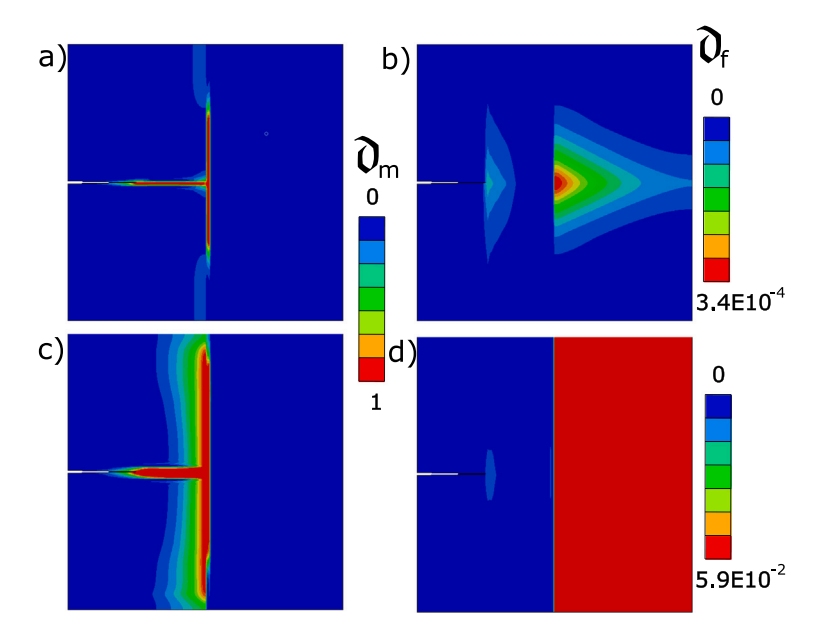


Fig. 19. Crack propagation of the bi-material interface with fiber orientation of 90°, along with the interplay between the fiber and matrix failure.

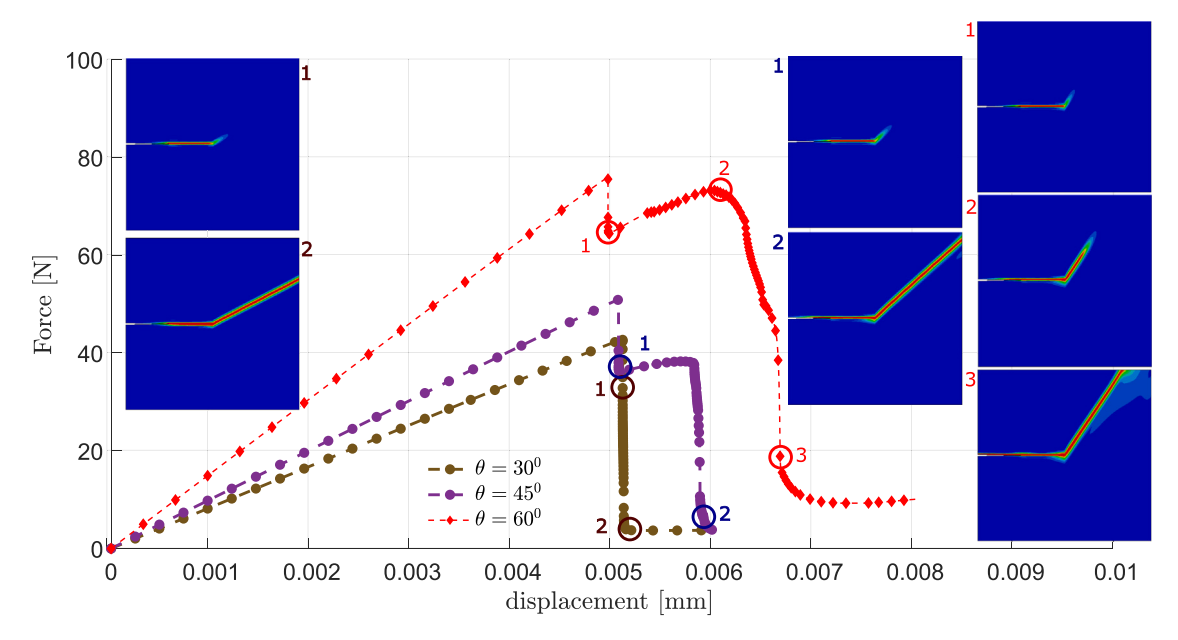


Fig. 20. Force vs. displacement plots for the bi-material interface with crack propagation for the fiber orientation of  $0-30^{\circ},\ 0-45^{\circ},\ and\ 0-60^{\circ}.$ 

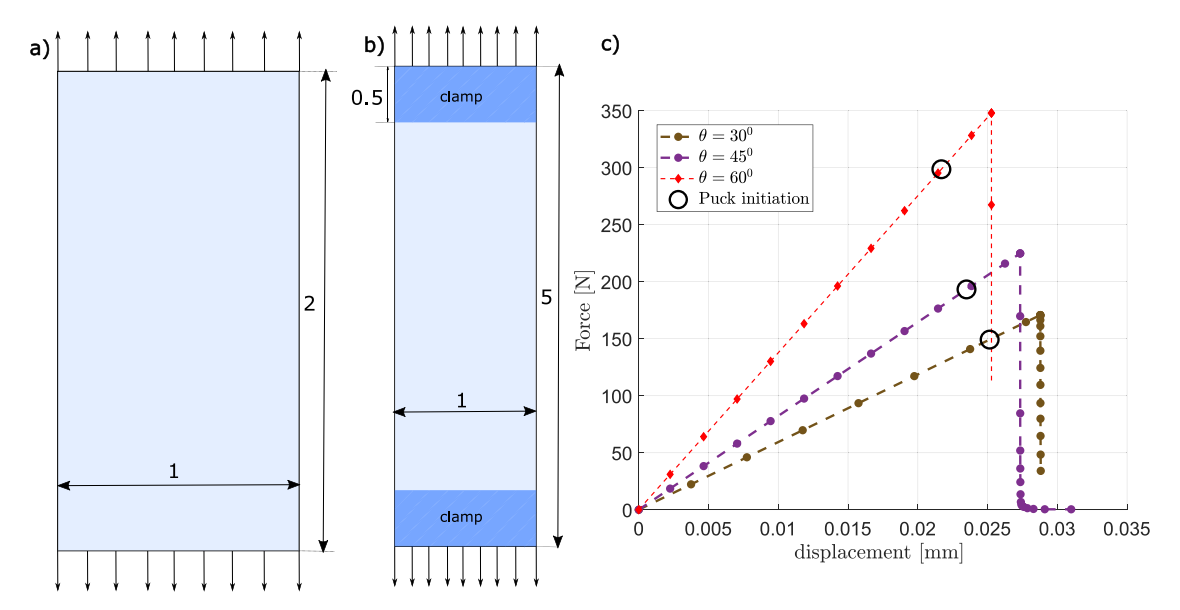


Fig. 21. (a) Geometric description of the tension in unnotched specimen used for the fiber orientation of 0°, and 90°, and (b) presents the geometrical description for fiber orientations of 30°, 45°, and 60°. (c) Representative force vs. displacement curves along with the Puck failure initiation.

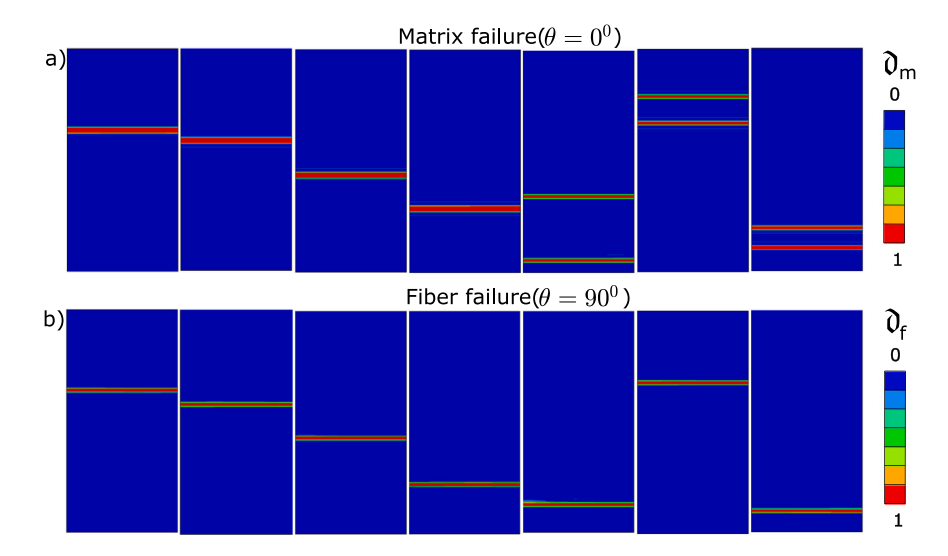


Fig. 22. (a) Matrix failure in different regions due to different configurations for the fiber orientation of  $0^{\circ}$ , and (b) presents the fiber failure in different regions due to different configurations for the fiber orientation of  $90^{\circ}$ .

case, the top and bottom parts of the geometry contain a material with very high stiffness and fracture toughness, as shown in Fig. 21(b). It is further noted that, stiff clamp has no effects on the crack propagation if the defect points are far away from the boundaries. Furthermore, the cracks originating from the boundary are discarded in this section.

Fifteen different random distributions of micro-cracks are planted in each model for each fiber orientation. Each distribution consists of the six micro-defects in the form of reduced fracture energy (5%–10%) assigned at random element. It is further noticed that, reducing the strength or reducing fracture energy lead to same results both qualitatively and quantitatively. Consequence, fracture energy is chosen in this article. Furthermore, only seven numerical simulations are shown here to maintain the conciseness of the article. The nucleation and the coalesce for each of the samples are omitted for the sake of brevity. The material properties considered are presented in Tables 1–4 with length scales taken as  $\ell_f=0.05~{\rm mm}$  and  $\ell_m=0.25~{\rm mm}$ .

Fig. 22(a) presents the matrix failure for the fibers oriented in  $0^{\circ}$ . Seven configurations show different possibilities for damage in line with the experimental observations. It is interesting to see that, in the

last three configurations, two matrix dominated cracks are seen. In all these configurations, only one crack is formed initially, followed a an unstable crack propagation of the second one. This could either indicate volatility of the matrix dominated damage or numerical instability stemming from the unstable crack propagation. Furthermore, Fig. 22(b) presents the fiber failure for the fiber oriented in 90°. Consequently, the load-carrying capacity for the structures with fiber orientations of 90° is higher. Additionally, it is noticed that in both cases, the microcracks are formed first, followed by a coalesce between these cracks, followed by unstable crack propagation.

Fig. 23(a), (b) and (c) presents the different crack paths for the fibers with the orientation of  $30^{\circ}$ ,  $45^{\circ}$ , and  $60^{\circ}$  respectively. In all these cases, only matrix-dominated failure is observed with no fiber damage, while the crack path is parallel to the fibers. Fig. 21(b) presents the force vs. displacement curve along with the Puck initiation. The early onset of the Puck initiation is approximately calculated as 10-12% less than the total load-carrying capacity due to the reduced fracture energy owing to artificial defects. Furthermore, due to the unstable crack propagation, in all the fifteen randomly distributed samples for

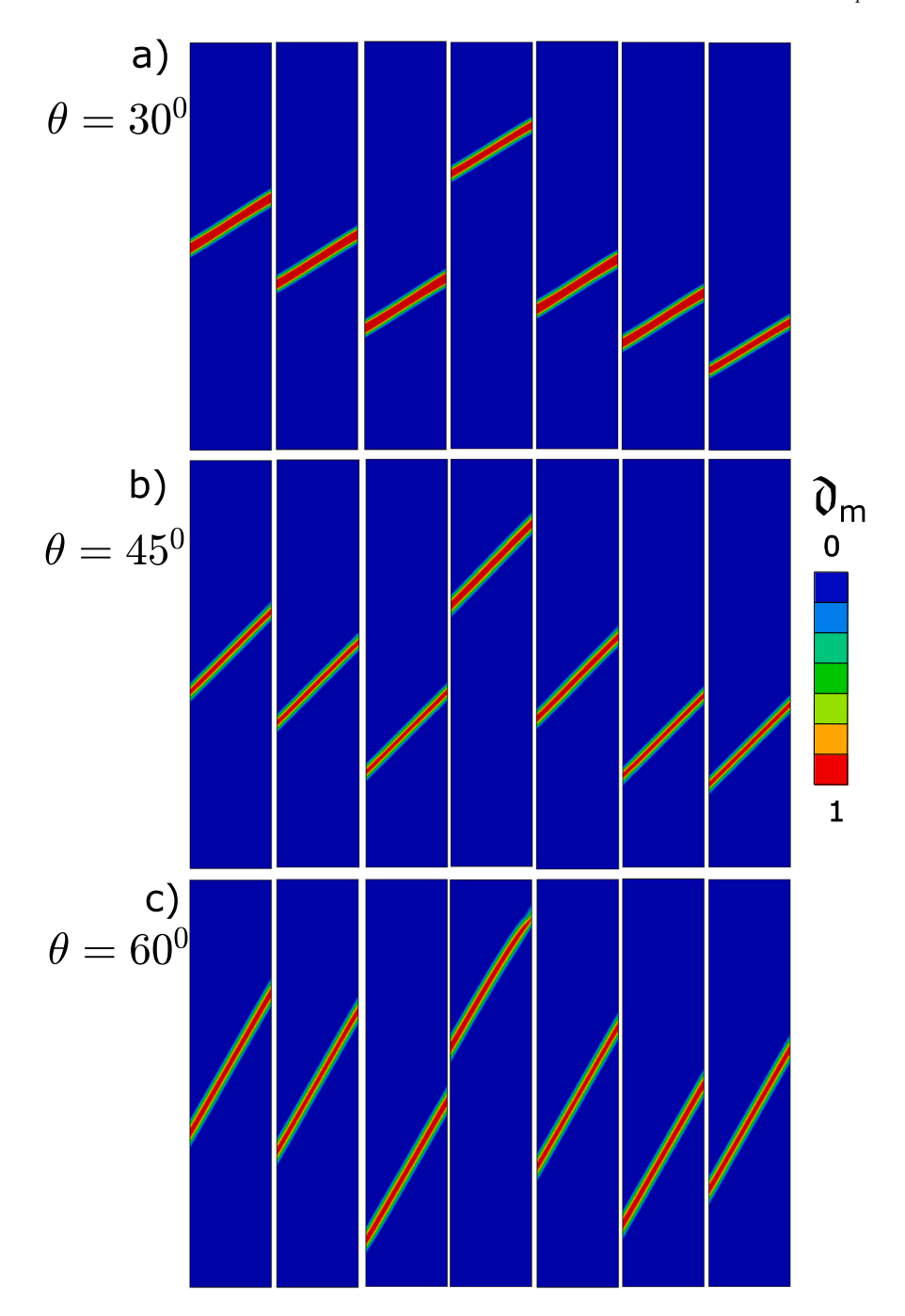


Fig. 23. Matrix failure in different regions due to the different configurations for the fiber orientation of (a) 30°, (b) 45°, and (c) 60°.

each fiber orientation, the difference in the force vs. displacement curves is less than 2%. Consequently, only one representative force vs. displacement curve for each fiber orientation is presented here for the sake of brevity.

## 7. Convergence studies

All simulations presented in this work were performed using six cores and employed the automatic time-stepping feature available in the Abaqus/Standard solver. The analyses were carried out with NL–GEOM=ON, using a Newton–Raphson solver with the stabilize option enabled. Time step cutbacks were permitted after 300 iterations, with a minimum time stepping increment of  $1\times 10^{-10}$  and a maximum of  $1\times 10^{-3}$ .

During crack propagation phases, occasional cutbacks in the time increment were observed. Table 6 presents the total computational time for each simulation associated with experimental comparison benchmarks, offering a practical estimate of solver performance.

While the current implicit implementation exhibits robust convergence, it is worth noting that explicit formulations as showed in [92] demonstrated improved computational efficiency and scalability for large-scale fracture problems. Exploring such explicit approaches with the present model is a valuable direction for future development.

## 8. Conclusion

A multi-phase field damage model capable of handling damage in both fiber and inter-fiber failure separately is proposed in this article.

**Table 6**Summary of the total time for the simulations.

Geometry	Orientation $(\theta)$	Total DOF	Total time (min)
Plate with Notch	0	193 844	63.31
	45		75.43
	90		27.16
Compact Tension	0	149 856	709.7
•	45		413.71
	90		214.892
Open Hole Tension	0	51 980	437.05
_	45		43.61
	90		28.73
Centered Notch	0	63 268	53.81
Tension	45		40.73
	90		43.28

The article utilizes the Puck failure theory for the crack initiation based on the local stress state, whereas the phase-field method propagates the crack. The directional nature of the fracture energy stemming from the various fiber orientations is considered for effective crack propagation. The first four examples show the model's ability to replicate qualitative and quantitative experimental results. In contrast, the last three examples show the model's ability to predict crack propagation in complex experimental settings.

An overall analysis of the Puck initiation suggests that each example can be fairly categorized into two parts. In examples such as OHT, TPB, and unnotched tension specimens, the Puck failure criteria are immediately followed by crack nucleation and propagation, consequently leading to a drop in reactions as soon as the Puck failure criteria are fulfilled. On the other hand, for the other examples, such as SENT, CNT, Bi-material interface, and CT, the Puck initiation is followed by a fairly long nucleation with subsequent crack propagation. Consequently, the quantitative analysis for the first case can be done with any driving force. In contrast, for the second case, the parameters  $\zeta_m$  and  $\zeta_f$  can control the driving force, providing an extensive range of flexibility for both qualitative and quantitative analysis of the FRCs.

Furthermore, the interplay between the fiber and the matrix failure is shown in two different contexts: (a) pure fiber failure (Unnotched tension), and (b) the effects of the fiber failure on the matrix (TBP, CT) are presented to show the ability of the model to understand fracture in FRCs effectively.

Due to the two-dimensional nature of the model, the model cannot capture out-of-plane cracks and delamination between the plies. Furthermore, when the Puck criteria are followed by a long nucleation phase, the parameters  $\zeta_m$   $\zeta_f$  need to be calibrated to capture the nucleation.

Finally, this work brings many benchmark examples together in the FRCs. Furthermore, the codes written in ABAQUS UEL and the input files are presented in the data availability section to alleviate the reproducibility crisis and bring transparency to the work.

## CRediT authorship contribution statement

Pavan Kumar Asur Vijaya Kumar: Writing – original draft, Formal analysis, Conceptualization. Rafael Fleischhacker: Visualization, Validation, Software. Aamir Dean: Software, Data curation, Conceptualization. Raimund Rolfes: Writing – review & editing, Supervision. Heinz E. Pettermann: Writing – review & editing, Supervision, Resources.

#### Declaration of competing interest

The authors declare that they have no known competing financial interests or personal relationships that could have appeared to influence the work reported in this paper.

## Acknowledgment

The authors sincerely acknowledge the technical discussion and pictures of Compact tension from experimental work provided by Prof. Zoltán Major and Andreas Kapshammer from the Institute of Polymer Product Engineering, Johannes Kepler University, Linz, Austria.

The authors acknowledge TU Wien Bibliothek for financial support through its Open Access Funding Programme.

## Appendix A. Effect of matrix structural tensor

This section presents the effects of each structural tensor in the presented model. Consequently, four different models are considered as follows

- 1. Without both structural tensors, similar to [5]. i.e  $\mathcal{A}_f=\mathcal{A}_m=\mathbb{I}.$
- 2. We consider only the structural tensor corresponding to the fiber  $(A_f)$ , in the absence of the matrix structural tensor. i.e  $A_m = \mathbb{I}$ .
- 3. Only structural tensor corresponding to the matrix  $(A_m)$  in the absence of the fiber structural tensor as in [2]. i.e  $A_f = \mathbb{I}$ .
- 4. Present model with both structural tensors  $(A_f, A_m)$  are considered.

Fig. A.24 presents the comparison of the different models using the plate with the notch example as considered in Section 6.1 with the same boundary conditions and material properties with the fiber orientation of  $\theta=45^\circ$ . It is apparent from Fig. A.24 that Case-1 and Case-2 without the structural tensor corresponding to the matrix  $(\mathcal{A}_m)$  cannot predict crack propagation path. Case-3, which corresponds to only the matrix structural tensor and the present model (Case-4), can predict the crack propagation well.

In conclusion, only the structural tensor corresponding to the matrix  $(A_m)$  is sufficient to predict crack propagation correctly when the inter-fiber/matrix dominates the damage.

#### Appendix B. Effect of fiber structural tensor

This section presents the effects of the structural tensor corresponding to the fiber  $(\mathcal{A}_f)$ . Puck's failure criteria suggest that, in most cases, the fracture plane in the fiber is approximately perpendicular to the fiber direction. Consequently, the fiber failure is restricted to the direction perpendicular to the fiber [50]. The example considers Tension in unnotched specimens as in Section 6.7 corresponding to the case when the fibers are oriented parallel to the load application (with  $\theta=90^\circ$ ) leading to fiber failure. With the same boundary conditions and material properties, Fig. B.25 compares the crack initiation, coalescence, and propagation of the fiber failure in the plate without a notch. It can be seen that, in the absence of the structural tensor, the

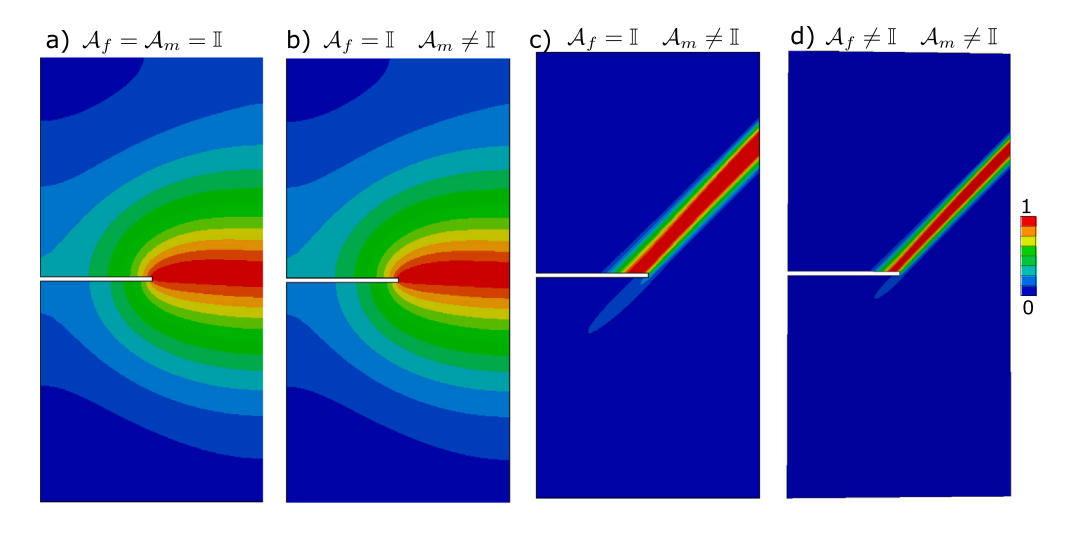


Fig. A.24. Comparison of the plate with notch sample with and without structural tensors.

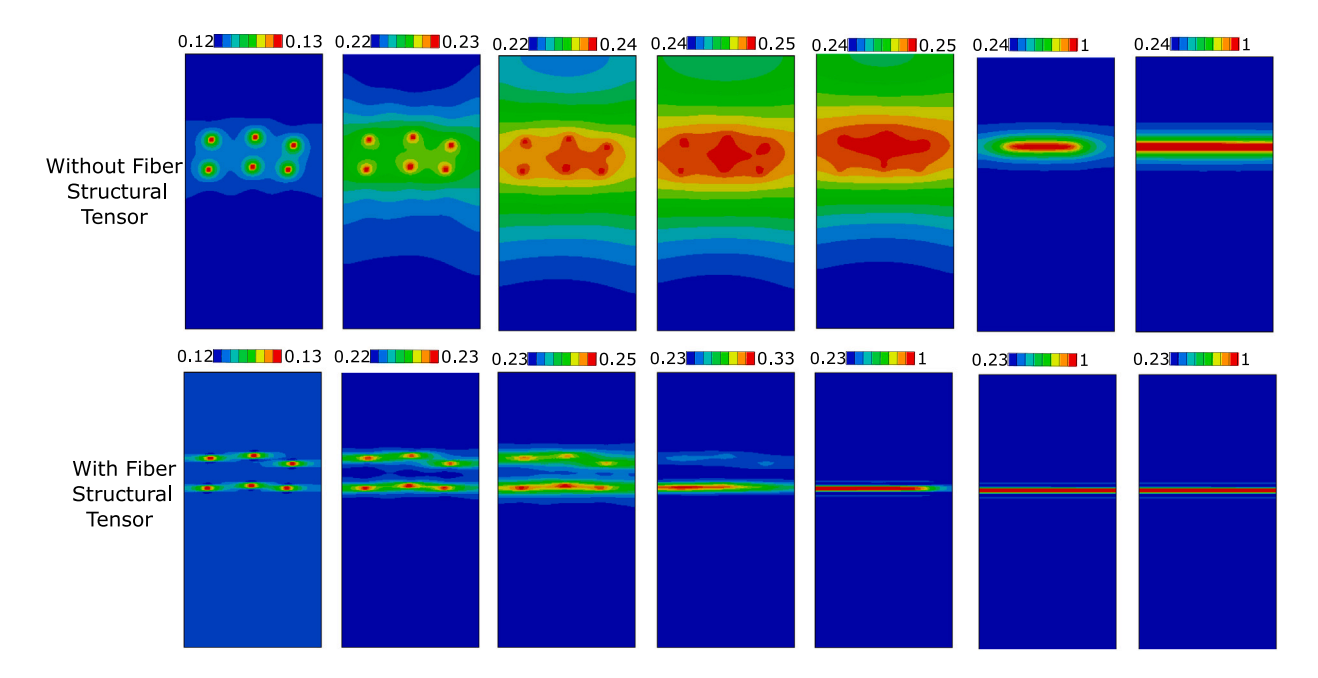


Fig. B.25. Comparison of fiber failure with crack initiation, coalescence, and propagation for a plate without a notch with and without a fiber structural tensor A<sub>f</sub>.

crack smears more. Furthermore, the crack coalescence leads to a thick band. Later, the coalescence leads to the localization of the stresses and crack propagation. The crack propagation is sharper in the presence of the structural tensor corresponding to the fiber  $(\mathcal{A}_f)$ . It is also observed that in the absence of  $\mathcal{A}_f$ , the load–displacement response is higher. It is important to note that Fig. B.25 only presents the fiber failure, while the matrix failure around the fibers is omitted for brevity.

Furthermore, it is also observed that in the laminates where the interaction between the fiber and inter-fiber failure is prominent, the model with structural tensor  $\mathcal{A}_f$  performs better in capturing the interactions.

## Appendix C. Single Edged Notched Tension

See Fig. C.26.

## Appendix D. Open hole tension

See Fig. D.27.

Appendix E. Compact tension

See Fig. E.28.

Appendix F. Three point bending

See Fig. F.29.

Appendix G. Bi-material interface

See Figs. G.30 and G.31.

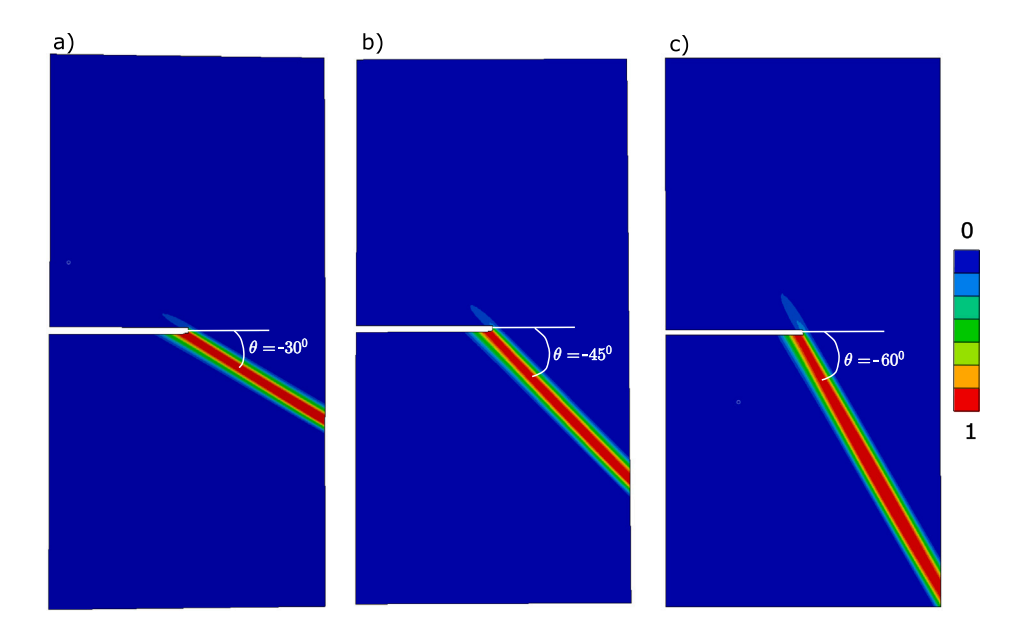


**Fig. C.26.** Crack propagation for the fiber orientation of (a)  $\theta = -30^{\circ}$ , (b)  $\theta = -45^{\circ}$ , (c)  $\theta = -60^{\circ}$ .

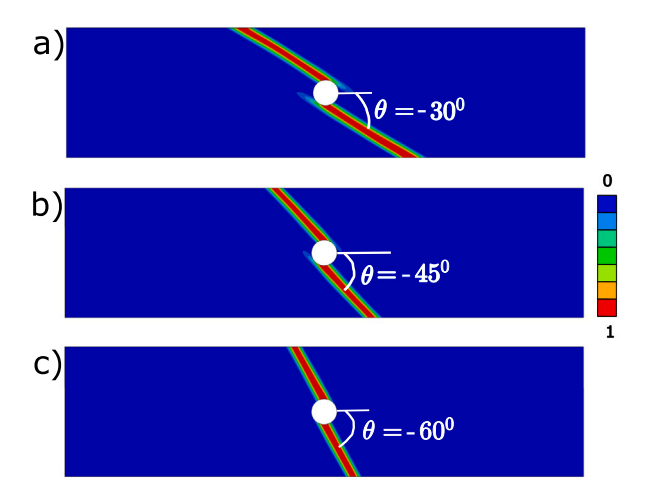


Fig. D.27. Crack propagation in open hole tension for the fiber angles of (a)  $\theta = -30^{\circ}$ , (b)  $\theta = -45^{\circ}$ , (c)  $\theta = -60^{\circ}$ .

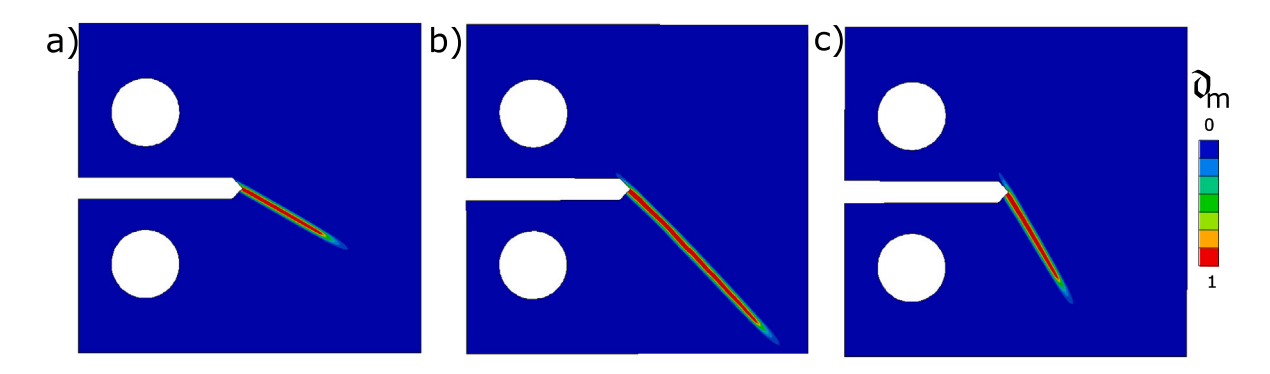


Fig. E.28. Crack propagation in compact tension specimen for the fiber orientation of (a) -30°, (b) -45°, and (c) -60°.

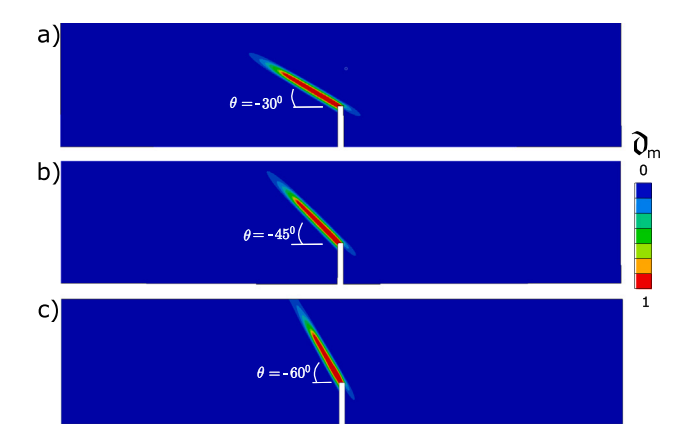


Fig. F.29. Crack propagation in three-point bending specimen with fiber orientation of (a) -30°, (b) -45°, and (c) -60°.

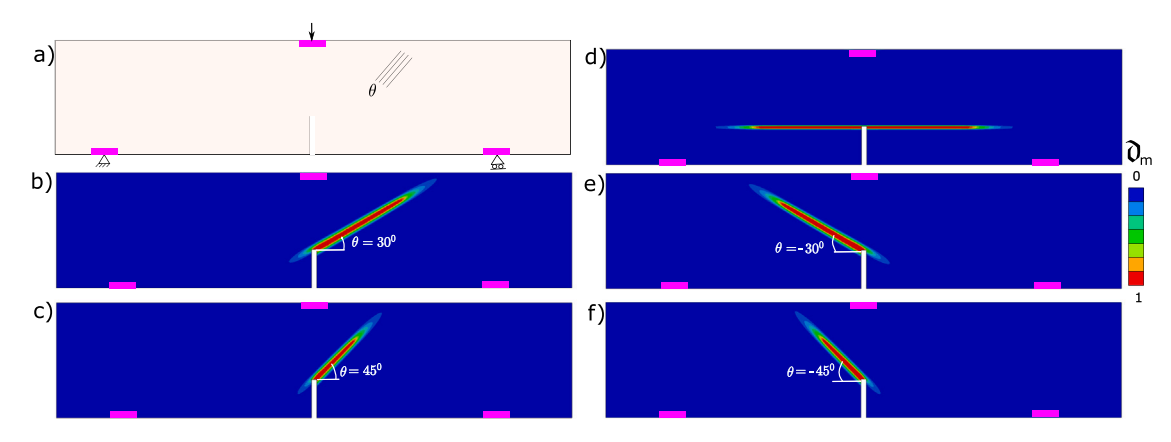


Fig. G.30. Crack propagation in three-point bending examples with stiff load boundaries for different fiber orientations.

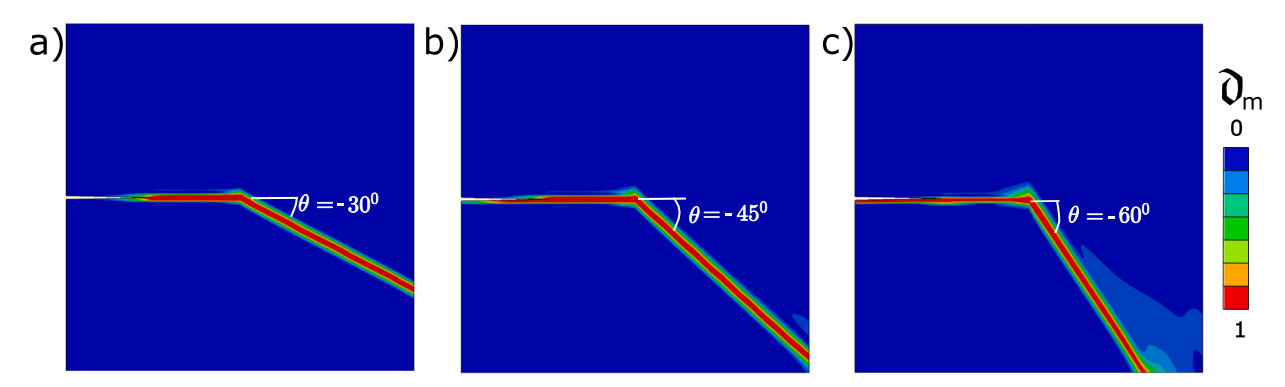


Fig. G.31. Crack propagation in the bi-material interface for the fiber orientation of second layer of (a) -30°, (b) -45°, and (c) -60°.

## Data availability

The codes used for this paper, including the input files and the FORTRAN codes can be downloaded from the following GitHub link: https://github.com/Pavan-asur/Multi-phase-field-Puck-FRC.

## References

- [1] Bui TQ, Hu X. A review of phase-field models, fundamentals and their applications to composite laminates. Eng Fract Mech 2021;248:107705. http://dx.doi. org/10.1016/j.engfracmech.2021.107705.
- [2] Zhang P, Hu X, Bui TQ, Yao W. Phase field modeling of fracture in fiber reinforced composite laminate. Int J Mech Sci 2019;161–162:105008. http://dx. doi.org/10.1016/j.ijmecsci.2019.07.007, URL https://www.sciencedirect.com/ science/article/pii/S0020740318341729.

- [3] Mrunmayee S, Rajagopal A, Rakesh K, Basant K, Reddy J. Phase field approach to predict mixed-mode delamination and delamination migration in composites. Compos Struct 2024;337:118074. http://dx.doi.org/10.1016/ j.compstruct.2024.118074, URL https://www.sciencedirect.com/science/article/ pii/S0263822324002022.
- [4] Pranavi D, Rajagopal A, Reddy J. Interaction of anisotropic crack phase field with interface cohesive zone model for fiber reinforced composites. Compos Struct 2021;270:114038. http://dx.doi.org/10.1016/j.compstruct.2021.114038, URL https://www.sciencedirect.com/science/article/pii/S0263822321004980.
- [5] Dean A, Asur Vijaya Kumar P, Reinoso J, Gerendt C, Paggi M, Mahdi E, et al. A multi phase-field fracture model for long fiber reinforced composites based on the Puck theory of failure. Compos Struct 2020;251:112446. http: //dx.doi.org/10.1016/j.compstruct.2020.112446.
- [6] Asur Vijaya Kumar P, Dean A, Reinoso J, Paggi M. A multi phase-field-cohesive zone model for laminated composites: Application to delamination migration. Compos Struct 2021;276:114471. http://dx.doi.org/10.1016/j.compstruct.2021. 114471.

- [7] Quintanas-Corominas A, Reinoso J, Casoni E, Turon A, Mayugo J. A phase field approach to simulate intralaminar and translaminar fracture in long fiber composite materials. Compos Struct 2019;220:899–911. http://dx.doi.org/10.1016/ j.compstruct.2019.02.007, URL https://www.sciencedirect.com/science/article/ pii/S0263822318339928.
- [8] Griffith AA. The phenomena of rupture and flow in solids. Philos Trans R Soc Lond 1921:221:163–98.
- [9] Francfort G, Marigo J-J. Revisiting brittle fracture as an energy minimization problem. J Mech Phys Solids 1998;46(8):1319–42. http://dx.doi.org/10.1016/ S0022-5096(98)00034-9.
- [10] Bourdin B, Francfort G, Marigo J-J. Numerical experiments in revisited brittle fracture. J Mech Phys Solids 2000;48(4):797–826. http://dx.doi.org/10.1016/ S0022-5096(99)00028-9.
- [11] Wu J-Y, Nguyen VP, Nguyen CT, Sutula D, Sinaie S, Bordas SP. In: Bordas SP, Balint DS, editors. Chapter One Phase-field modeling of fracture. Advances in applied mechanics, vol. 53, Elsevier; 2020, p. 1–183. http://dx.doi.org/10.1016/bs.aams.2019.08.001, URL https://www.sciencedirect.com/science/article/pii/S0065215619300134.
- [12] Lopez-Pamies O, Dolbow JE, Francfort GA, Larsen CJ. Classical variational phase-field models cannot predict fracture nucleation. Comput Methods Appl Mech Engrg 2025;433:117520. http://dx.doi.org/10.1016/j.cma.2024.117520, URL https://www.sciencedirect.com/science/article/pii/S0045782524007746.
- [13] Asur Vijaya Kumar PK, Anam K, Pettermann HE, Paggi M. Gradient-scaled phase field approach to fracture for size-scale and shape-effects. 2024, http: //dx.doi.org/10.2139/ssrn.4883944, Submitted to CMAME.
- [14] Miehe C, Welschinger F, Hofacker M. Thermodynamically consistent phase-field models of fracture: Variational principles and multi-field FE implementations. Internat J Numer Methods Engrg 2010;83(10):1273–311. http://dx.doi. org/10.1002/nme.2861, arXiv:https://onlinelibrary.wiley.com/doi/pdf/10.1002/ nme.2861. URL https://onlinelibrary.wiley.com/doi/abs/10.1002/nme.2861.
- [15] Schlüter A, Willenbücher A, Kuhn C, Müller R. Phase field approximation of dynamic brittle fracture. Comput Mech 2014;54(5):1141–61. http://dx.doi.org/ 10.1007/s00466-014-1045-x.
- [16] Msekh MA, Sargado JM, Jamshidian M, Areias PM, Rabczuk T. Abaqus implementation of phase-field model for brittle fracture. Comput Mater Sci 2015;96:472–84. http://dx.doi.org/10.1016/j.commatsci.2014.05.071, Special Issue Polymeric Composites, URL https://www.sciencedirect.com/science/article/ pii/S0927025614004133.
- [17] Miehe C, Hofacker M, Welschinger F. A phase field model for rate-independent crack propagation: Robust algorithmic implementation based on operator splits. Comput Methods Appl Mech Engrg 2010;199(45):2765–78. http://dx.doi.org/10. 1016/j.cma.2010.04.011, URL https://www.sciencedirect.com/science/article/ pii/S0045782510001283.
- [18] Mesgarnejad A, Bourdin B, Khonsari M. Validation simulations for the variational approach to fracture. Comput Methods Appl Mech Engrg 2015;290:420–37. http: //dx.doi.org/10.1016/j.cma.2014.10.052, URL https://www.sciencedirect.com/ science/article/pii/S004578251400423X.
- [19] Freddi F, Iurlano F. Numerical insight of a variational smeared approach to cohesive fracture. J Mech Phys Solids 2017;98:156–71. http://dx.doi.org/10. 1016/j.jmps.2016.09.003, URL https://www.sciencedirect.com/science/article/ pii/S0022509616304860.
- [20] Paggi M, Reinoso J. Revisiting the problem of a crack impinging on an interface: A modeling framework for the interaction between the phase field approach for brittle fracture and the interface cohesive zone model. Comput Methods Appl Mech Engrg 2017;321:145–72. http://dx.doi.org/10.1016/j.cma.2017.04.004, URL https://www.sciencedirect.com/science/article/pii/S0045782516317066.
- [21] Wu J-Y. A unified phase-field theory for the mechanics of damage and quasi-brittle failure. J Mech Phys Solids 2017;103:72–99. http://dx.doi.org/10. 1016/j.jmps.2017.03.015, URL https://www.sciencedirect.com/science/article/ pii/S0022509616308341.
- [22] Nguyen T, Yvonnet J, Zhu Q-Z, Bornert M, Chateau C. A phase-field method for computational modeling of interfacial damage interacting with crack propagation in realistic microstructures obtained by microtomography. Comput Methods Appl Mech Engrg 2016;312:567–95. http://dx.doi.org/10.1016/j.cma.2015.10.007, Phase Field Approaches to Fracture, URL https://www.sciencedirect.com/science/article/pii/S0045782515003266.
- [23] Conti S, Focardi M, Iurlano F. Phase field approximation of cohesive fracture models. Ann Inst Henri Poincaré C Anal Non Linéaire 2016;33(4):1033–67. http://dx.doi.org/10.1016/j.anihpc.2015.02.001, URL https://www.sciencedirect.com/science/article/pii/S0294144915000360.
- [24] Borden MJ, Verhoosel CV, Scott MA, Hughes TJ, Landis CM. A phase-field description of dynamic brittle fracture. Comput Methods Appl Mech Engrg 2012;217–220:77–95. http://dx.doi.org/10.1016/j.cma.2012.01.008, URL https://www.sciencedirect.com/science/article/pii/S0045782512000199.
- [25] Bourdin B, Larsen CJ, Richardson CL. A time-discrete model for dynamic fracture based on crack regularization. Int J Fract 2011;168(2):133–43. http://dx.doi.org/ 10.1007/s10704-010-9562-x.
- [26] Doan DH, Bui TQ, Van Do T, Duc ND. A rate-dependent hybrid phase field model for dynamic crack propagation. J Appl Phys 2017;122(11):115102. http: //dx.doi.org/10.1063/1.4990073, arXiv:https://pubs.aip.org/aip/jap/article-pdf/ doi/10.1063/1.4990073/13334518/115102\_1\_online.pdf.

- [27] Zhou S, Zhuang X, Rabczuk T. Phase-field modeling of fluid-driven dynamic cracking in porous media. Comput Methods Appl Mech Engrg 2019;350:169–98. http://dx.doi.org/10.1016/j.cma.2019.03.001, URL https://www.sciencedirect. com/science/article/pii/S0045782519301276.
- [28] Nguyen VP, Wu J-Y. Modeling dynamic fracture of solids with a phase-field regularized cohesive zone model. Comput Methods Appl Mech Engrg 2018;340:1000–22. http://dx.doi.org/10.1016/j.cma.2018.06.015, URL https://www.sciencedirect.com/science/article/pii/S004578251830313X.
- [29] Kristensen PK, Niordson CF, Martínez-Pañeda E. A phase field model for elastic-gradient-plastic solids undergoing hydrogen embrittlement. J Mech Phys Solids 2020;143:104093. http://dx.doi.org/10.1016/j.jmps.2020.104093.
- [30] Cui C, Bortot P, Ortolani M, Martínez-Pañeda E. Computational predictions of hydrogen-assisted fatigue crack growth. Int J Hydrog Energy 2024;72:315–25. http://dx.doi.org/10.1016/j.ijhydene.2024.05.264, URL https://www.sciencedirect.com/science/article/pii/S036031992401961X.
- [31] Martínez-Pañeda E, Golahmar A, Niordson CF. A phase field formulation for hydrogen assisted cracking. Comput Methods Appl Mech Engrg 2018;342:742–61. http://dx.doi.org/10.1016/j.cma.2018.07.021, URL https://www.sciencedirect.com/science/article/pii/S0045782518303529.
- [32] Miehe C, Hofacker M, Schänzel L-M, Aldakheel F. Phase field modeling of fracture in multi-physics problems. Part II. coupled brittle-to-ductile failure criteria and crack propagation in thermo-elastic-plastic solids. Comput Methods Appl Mech Engrg 2015;294:486–522. http://dx.doi.org/10.1016/j.cma.2014.11.
- [33] Kumar PKAV, Dean A, Sahraee S, Reinoso J, Paggi M. Non-linear thermoelastic analysis of thin-walled structures with cohesive-like interfaces relying on the solid shell concept. Finite Elem Anal Des 2022;202:103696. http://dx.doi.org/10. 1016/j.finel.2021.103696, URL https://www.sciencedirect.com/science/article/ pii/S0168874X21001700.
- [34] Asur Vijaya Kumar PK, Dean A, Reinoso J, Paggi M. Nonlinear thermo-elastic phase-field fracture of thin-walled structures relying on solid shell concepts. Comput Methods Appl Mech Engrg 2022;396:115096. http://dx.doi.org/10. 1016/j.cma.2022.115096, URL https://www.sciencedirect.com/science/article/ pii/S0045782522002936.
- [35] Bleyer J, Alessi R. Phase-field modeling of anisotropic brittle fracture including several damage mechanisms. Comput Methods Appl Mech Engrg 2018;336:213–36. http://dx.doi.org/10.1016/j.cma.2018.03.012, URL https://www.sciencedirect.com/science/article/pii/S0045782518301373.
- [36] Dean A, Reinoso J, Jha N, Mahdi E, Rolfes R. A phase field approach for ductile fracture of short fibre reinforced composites. Theor Appl Fract Mech 2020;106:102495. http://dx.doi.org/10.1016/j.tafmec.2020.102495, URL https: //www.sciencedirect.com/science/article/pii/S0167844219306536.
- [37] Wang Q, Feng Y, Zhou W, Cheng Y, Ma G. A phase-field model for mixed-mode fracture based on a unified tensile fracture criterion. Comput Methods Appl Mech Engrg 2020;370:113270. http://dx.doi.org/10.1016/j.cma.2020.113270, URL https://www.sciencedirect.com/science/article/pii/S0045782520304552.
- [38] Asur Vijaya Kumar P, Dean A, Reinoso J, Lenarda P, Paggi M. Phase field modeling of fracture in functionally graded materials: Γ -convergence and mechanical insight on the effect of grading. Thin-Walled Struct 2021;159:107234. http://dx.doi.org/10.1016/j.tws.2020.107234, URL https://www.sciencedirect.com/science/article/pii/S0263823120311046.
- [39] Alessi R, Freddi F. Phase-field modelling of failure in hybrid laminates. Compos Struct 2017;181:9–25. http://dx.doi.org/10.1016/j.compstruct.2017.08.073, URL https://www.sciencedirect.com/science/article/pii/S0263822317313107.
- [40] Reinoso J, Arteiro A, Paggi M, Camanho P. Strength prediction of notched thin ply laminates using finite fracture mechanics and the phase field approach. Compos Sci Technol 2017;150:205–16. http://dx.doi.org/10.1016/j. compscitech.2017.07.020, URL https://www.sciencedirect.com/science/article/ pii/S0266353817310552.
- [41] Hirshikesh, Natarajan S, Annabattula RK. Modeling crack propagation in variable stiffness composite laminates using the phase field method. Compos Struct 2019;209:424–33. http://dx.doi.org/10.1016/j.compstruct.2018.10.083, URL https://www.sciencedirect.com/science/article/pii/S0263822318325935.
- [42] Singh A, Pal S. Multi-phase field modeling for various fracture mechanisms in composites. Eng Fract Mech 2021;241:107348. http://dx.doi.org/10.1016/j. engfracmech.2020.107348, URL https://www.sciencedirect.com/science/article/ pii/S0013794420309292.
- [43] Zhang P, Yao W, Hu X, Bui TQ. An explicit phase field model for progressive tensile failure of composites. Eng Fract Mech 2021;241:107371. http://dx.doi. org/10.1016/j.engfracmech.2020.107371, URL https://www.sciencedirect.com/ science/article/pii/S0013794420309516.
- [44] Yue Q, Wang Q, Tian W, Rabczuk T, Zhou W, Ma G, et al. A phase-field lattice model (PFLM) for fracture problem: Theory and application in composite materials. Compos Struct 2023;323:117432. http://dx.doi.org/10.1016/ j.compstruct.2023.117432, URL https://www.sciencedirect.com/science/article/ pii/S026382232300778X.
- [45] Li P, Li W, Li B, Yang S, Shen Y, Wang Q, et al. A review on phase field models for fracture and fatigue. Eng Fract Mech 2023;289:109419. http://dx.doi.org/10. 1016/j.engfracmech.2023.109419, URL https://www.sciencedirect.com/science/ article/pii/S0013794423003776.

- [46] Hu X, Tan S, Xu H, Sun Z, Wang T, Min L, et al. Modelling high temperature progressive failure in C/SiC composites using a phase field model: Oxidation rate controlled process. Comput Methods Appl Mech Engrg 2025;433:117544. http://dx.doi.org/10.1016/j.cma.2024.117544, URL https://www.sciencedirect.com/science/article/pii/S0045782524007989.
- [47] Gültekin O, Dal H, Holzapfel GA. Numerical aspects of anisotropic failure in soft biological tissues favor energy-based criteria: A rate-dependent anisotropic crack phase-field model. Comput Methods Appl Mech Engrg 2018;331:23–52. http://dx.doi.org/10.1016/j.cma.2017.11.008.
- [48] Gültekin O, Dal H, Holzapfel G. A phase-field approach to model fracture of arterial walls: Theory and finite element analysis. Comput Methods Appl Mech Engrg 2016;312:542–66. http://dx.doi.org/10.1016/j.cma.2016.04.007.
- [49] Kamarei F, Dolbow J, Lopez-Pamies O. Nucleation of fracture: The first-octant evidence against classical variational phase-field models. J Appl Mech 2024;1–5. http://dx.doi.org/10.1115/1.4067146, arXiv:https://asmedigitalcollection.asme. org/appliedmechanics/article-pdf/doi/10.1115/1.4067146/7404104/jam-24-1344.pdf.
- [50] Puck A, Schürmann H. Failure analysis of FRP laminates by means of physically based phenomenological models. Compos Sci Technol 2002;62(12):1633–62. http://dx.doi.org/10.1016/S0266-3538(01)002081, URL http://www.sciencedirect.com/science/article/pii/S0266353801002081.
- [51] Hashin Z. Fatigue failure criteria for unidirectional fiber composites. J Appl Mech 1981;48(4):846–52. http://dx.doi.org/10.1115/1.3157744.
- [52] Pinho ST, Davila CG, Camanho PP, Iannucci L, Robinson P. Failure models and criteria for frp under in-plane or three-dimensional stress states including shear non-linearity. 2013.
- [53] Pinho S, Iannucci L, Pinh ST, Robinson P. Physically-based failure models and criteria for laminated fibre-reinforced composites with emphasis on fibre kinking: Part I: Development. Compos Part A: Appl Sci Manuf 2006;37(1):63–73. http://dx.doi.org/10.1016/j.compositesa.2005.04.016.
- [54] Pinho ST, Darvizeh R, Robinson P, Schuecker C, Camanho PP. Material and structural response of polymer-matrix fibre-reinforced composites. J Compos Mater 2012;46(19–20):2313–41. http://dx.doi.org/10.1177/0021998312454478.
- [55] Bullegas G, Lamela JM, Pimenta S, Pinho S. On the role of dynamic stress concentrations and fracture mechanics in the longitudinal tensile failure of fibrereinforced composites. Eng Fract Mech 2020;228:106920. http://dx.doi.org/10. 1016/j.engfracmech.2020.106920.
- [56] Laffan MJ, Pinho ST, Robinson P, Iannucci L, McMillan AJ. Measurement of the fracture toughness associated with the longitudinal fibre compressive failure mode of laminated composites. Compos Part A: Appl Sci Manuf 2012;43(11):1930–8. http://dx.doi.org/10.1016/j.compositesa.2012.04.009.
- [57] Laffan MJ, Pinho ST, Robinson P, McMillan AJ. Translaminar fracture toughness testing of composites: A review. Polym Test 2012;31(3):481–9. http://dx.doi.org/ 10.1016/j.polymertesting.2012.01.002.
- [58] Laffan MJ, Pinho ST, Robinson P, Iannucci L. Measurement of the in situ ply fracture toughness associated with mode I fibre tensile failure in frp. Part II: Size and lay-up effects. Compos Sci Technol 2010;70(4):614–21. http://dx.doi. org/10.1016/j.compscitech.2009.12.011.
- [59] Schasching MM, Červinek O, Koutný D, Pettermann HE, Todt M. A uniaxial hysteretic superelastic constitutive model applied to additive manufactured lattices. PAMM 2025;25(1):e202400092. http://dx.doi.org/10.1002/pamm.202400092, URL https://onlinelibrary.wiley.com/doi/abs/10.1002/pamm.202400092.
- [60] Kaul J, Pettermann H. A constitutive model for fiber reinforced polymer plies - implicit anisotropic evolution of damage and plasticity based on effective strengths. Compos Part C: Open Access 2021;4:100097. http://dx.doi.org/10. 1016/j.jcomc.2020.100097.
- [61] Ma R, Sun W. FFT-based solver for higher-order and multi-phase-field fracture models applied to strongly anisotropic brittle materials. Comput Methods Appl Mech Engrg 2020;362:112781. http://dx.doi.org/10.1016/j.cma.2019.112781.
- [62] Fei F, Choo J. Double-phase-field formulation for mixed-mode fracture in rocks. Comput Methods Appl Mech Engrg 2021;376:113655. http://dx.doi.org/ 10.1016/j.cma.2020.113655.
- [63] Doan DH, Van Do T, Nguyen NX, Van Vinh P, Trung NT. Multi-phase-field modelling of the elastic and buckling behaviour of laminates with ply cracks. Appl Math Model 2021;94:68–86. http://dx.doi.org/10.1016/j.apm.2020.12.038.
- [64] Gerendt C, Dean A, Mahrholz T, Englisch N, Krause S, Rolfes R. On the progressive fatigue failure of mechanical composite joints: Numerical simulation and experimental validation. Compos Struct 2020;248:112488. http://dx.doi.org/ 10.1016/j.compstruct.2020.112488.
- [65] Zou X, Xu Z, Gao J, Wu S, Li R, Li W, et al. An explicit multi-phase field damage model for long fiber-reinforced composites. Compos Struct 2023;309:116737. http://dx.doi.org/10.1016/j.compstruct.2023.116737.
- [66] Paggi M, Corrado M, Reinoso J. Fracture of solar-grade anisotropic polycrystalline silicon: A combined phase field-cohesive zone model approach. Comput Methods Appl Mech Engrg 2018;330:123–48. http://dx.doi.org/10.1016/j.cma. 2017.10.021.
- [67] Zhang P, Yao W, Hu X, Bui TQ. 3D micromechanical progressive failure simulation for fiber-reinforced composites. Compos Struct 2020;249:112534. http://dx.doi.org/10.1016/j.compstruct.2020.112534, URL https://www.sciencedirect.com/science/article/pii/S0263822319348421.

- [68] Zhang P, Tan S, Hu X, Yao W, Zhuang X. A double-phase field model for multiple failures in composites. Compos Struct 2022;293:115730. http:// dx.doi.org/10.1016/j.compstruct.2022.115730, URL https://www.sciencedirect. com/science/article/pii/S0263822322005074.
- [69] Jain I, Muixí A, Annavarapu C, Mulay SS, Rodríguez-Ferran A. Adaptive phase-field modeling of fracture in orthotropic composites. Eng Fract Mech 2023;292:109673. http://dx.doi.org/10.1016/j.engfracmech.2023.109673, URL https://www.sciencedirect.com/science/article/pii/S0013794423006318.
- [70] Min L, Hu X, Yao W, Bui TQ, Zhang P. On realizing specific failure initiation criteria in the phase field model. Comput Methods Appl Mech Engrg 2022;394:114881. http://dx.doi.org/10.1016/j.cma.2022.114881, URL https://www.sciencedirect.com/science/article/pii/S0045782522001773.
- [71] Li P, Yvonnet J, Wu Y. Improved fracture resistance of 3D-printed elastoplastic structures with respect to their topology and orientation of deposited layers. Int J Mech Sci 2022;220:107147. http://dx.doi.org/10.1016/j.ijmecsci.2022.107147, URL https://www.sciencedirect.com/science/article/pii/S0020740322000777.
- [72] Pan Z, Liew K. Predicting vibration characteristics of rotating composite blades containing CNT-reinforced composite laminae and damaged fiber-reinforced composite laminae. Compos Struct 2020;250:112580. http://dx.doi.org/10.1016/ j.compstruct.2020.112580, URL https://www.sciencedirect.com/science/article/ pii/S0263822320320419.
- [73] Pan Z, Zhang L-W, Liew K. Adaptive surrogate-based harmony search algorithm for design optimization of variable stiffness composite materials. Comput Methods Appl Mech Engrg 2021;379:113754. http://dx.doi.org/10.1016/j.cma.2021.113754, URL https://www.sciencedirect.com/science/article/pii/S0045782521000906.
- [74] Pan Z, Zhang L, Liew K. A phase-field framework for failure modeling of variable stiffness composite laminae. Comput Methods Appl Mech Engrg 2022;388:114192. http://dx.doi.org/10.1016/j.cma.2021.114192, URL https:// www.sciencedirect.com/science/article/pii/S0045782521005235.
- [75] Deuschle HM, Kröplin B-H. Finite element implementation of Puck's failure theory for fibre-reinforced composites under three-dimensional stress. J Compos Mater 2012;46(19–20):2485–513. http://dx.doi.org/10.1177/ 0021998312451480.
- [76] Cahill L, Natarajan S, Bordas S, O'Higgins R, McCarthy C. An experimental/numerical investigation into the main driving force for crack propagation in uni-directional fibre-reinforced composite laminae. Compos Struct 2014;107:119–30. http://dx.doi.org/10.1016/j.compstruct.2013.05.039, URL https://www.sciencedirect.com/science/article/pii/S0263822313002584.
- [77] Hirshikesh, Martínez-Pañeda E, Natarajan S. Adaptive phase field modelling of crack propagation in orthotropic functionally graded materials. Def Technol 2021;17(1):185–95. http://dx.doi.org/10.1016/j.dt.2020.03.004, URL https: //www.sciencedirect.com/science/article/pii/S221491471931342X.
- [78] Prabhakar P, Waas AM. A novel continuum-decohesive finite element for modeling in-plane fracture in fiber reinforced composites. Compos Sci Technol 2013;83:1–10. http://dx.doi.org/10.1016/j.compscitech.2013.03.022, URL https://www.sciencedirect.com/science/article/pii/S0266353813001450.
- [79] Kumar A, Sain T. Phase field-based cohesive zone approach to model delamination in fiber-reinforced polymer composites. Compos Struct 2024;329:117751. http://dx.doi.org/10.1016/j.compstruct.2023.117751, URL https://www.sciencedirect.com/science/article/pii/S0263822323010978.
- [80] Hallett S, Green B, Jiang W, Wisnom M. An experimental and numerical investigation into the damage mechanisms in notched composites. Compos Part A: Appl Sci Manuf 2009;40(5):613–24. http://dx.doi.org/10.1016/ j.compositesa.2009.02.021, URL https://www.sciencedirect.com/science/article/ pii/S1359835X09000499.
- [81] Felger J, Stein N, Becker W. Mixed-mode fracture in open-hole composite plates of finite-width: An asymptotic coupled stress and energy approach. Int J Solids Struct 2017;122–123:14–24. http://dx.doi.org/10.1016/j.ijsolstr.2017.05.039, URL https://www.sciencedirect.com/science/article/pii/S0020768317302524.
- [82] Flatscher T, Wolfahrt M, Pinter G, Pettermann H. Simulations and experiments of open hole tension tests – Assessment of intra-ply plasticity, damage, and localization. Compos Sci Technol 2012;72(10):1090–5. http://dx.doi.org/10.1016/ j.compscitech.2011.07.021, URL https://www.sciencedirect.com/science/article/ pii/S0266353811002740.
- [83] Jose S, Ramesh Kumar R, Jana M, Venkateswara Rao G. Intralaminar fracture toughness of a cross-ply laminate and its constituent sub-laminates. Compos Sci Technol 2001;61(8):1115–22. http://dx.doi.org/10.1016/S0266-3538(01)00011-2, URL https://www.sciencedirect.com/science/article/pii/S0266353801000112.
- [84] Kumar A, Sain T. A 3D multi-phase-field model for orientation-dependent complex crack interaction in fiber-reinforced composite laminates. Eng Fract Mech 2024;303:110097. http://dx.doi.org/10.1016/j.engfracmech.2024.110097.
- [85] Nonn SD. Effects of defects and damage localization in carbon fiber reinforced polymer lightweight structures. 2018, URL https://resolver.obvsg.at/urn:nbn:at: at-ubl:1-24676.
- [86] Adams R, Cawley P. A review of defect types and nondestructive testing techniques for composites and bonded joints. NDT Int 1988;21(4):208–22. http://dx.doi.org/10.1016/0308-9126(88)90333-1, URL https://www.sciencedirect.com/science/article/pii/0308912688903331.

- [87] Hörrmann S, Adumitroaie A, Schagerl M. Through-thickness fatigue behavior of non-crimp fabrics featuring manufacturing defects. Procedia Struct Integr 2016;2:158-65. http://dx.doi.org/10.1016/j.prostr.2016.06.021, 21st European Conference on Fracture, ECF21, 20-24 June 2016, Catania, Italy, URL https: //www.sciencedirect.com/science/article/pii/S245232161630021X.
- [88] Hörrmann S, Adumitroaie A, Schagerl M. The effect of ply folds as manufacturing defect on the fatigue life of CFRP materials. Fract Struct Integr 2016;10(38):Pages 76–81. http://dx.doi.org/10.3221/IGF-ESIS.38.10, URL https://www.fracturae. com/index.php/fis/article/view/1772.
- [89] Hörrmann S, Adumitroaie A, Viechtbauer C, Schagerl M. The effect of fiber waviness on the fatigue life of CFRP materials. Int J Fatigue 2016;90:139–47. http://dx.doi.org/10.1016/j.ijfatigue.2016.04.029, URL https://www.sciencedirect.com/science/article/pii/S0142112316300834.
- [90] Nonn S, Kralovec C, Schagerl M. Damage mechanisms under static and fatigue loading at locally compacted regions in a high pressure resin transfer molded carbon fiber non-crimp fabric. Compos Part A: Appl Sci Manuf 2018;115:57–65. http://dx.doi.org/10.1016/j.compositesa.2018.09.011, URL https://www.sciencedirect.com/science/article/pii/S1359835X18303610.
- [91] Nonn S, Schagerl M, Zhao Y, Gschossmann S, Kralovec C. Application of electrical impedance tomography to an anisotropic carbon fiber-reinforced polymer composite laminate for damage localization. Compos Sci Technol 2018;160:231–6. http://dx.doi.org/10.1016/j.compscitech.2018.03.031, URL https://www.sciencedirect.com/science/article/pii/S026635381733186X.
- [92] Hu X, Tan S, Xia D, Min L, Xu H, Yao W, et al. An overview of implicit and explicit phase field models for quasi-static failure processes, implementation and computational efficiency. Theor Appl Fract Mech 2023;124:103779. http:// dx.doi.org/10.1016/j.tafmec.2023.103779, URL https://www.sciencedirect.com/ science/article/pii/S0167844223000319.